scientific reports

OPEN

Steric and energetic studies on adsorption of toxic arsenic ions by hematite nano-rods from laterite highlighting the impact of modification periods

Dina Mostafa[1], **Nabila Shehata**[1,2], **Mashael D. Alqahtani**[3], **May N. Bin Jumah**[3], **Nahaa M. Alotaibi**[3], **Noof A. Alenazi**[4], **Hassan A. Rudayni**[5], **Ahmed A. Allam**[5], **Wail Al Zoubi**[6]✉ & **Mostafa R. Abukhadra**[7,8]

This study presents a facile, cost-effective hydrothermal transformation of natural lateritic iron ore into hematite nanorods, offering significant economic and technical benefits for the remediation of toxic arsenic ions. Lateritic iron ore was subjected to alkaline modification for different durations (12 h (HM12), 24 h (HM24), 36 h (HM36), and 48 h (HM48)), leading to morphological evolution into nanorod structures (2D) with variations in surface area, crystallinity, and adsorption efficacy for arsenate (As(V)) ions. Comprehensive characterization confirmed significant structural and physicochemical modifications. X-ray diffraction (XRD) analysis revealed a shift in peak positions and intensity reduction, indicative of lattice strain and increased surface defects. Fourier-transform infrared spectroscopy (FT-IR) confirmed modifications in the Fe–O coordination, and Brunauer–Emmett–Teller (BET) surface area analysis demonstrated a notable increase in surface area, with HM36 exhibiting the highest value (154.7 m^2/g). Adsorption experiments indicated that HM36 achieved the highest As(V) removal capacity (151.4 mg/g), followed by HM48 (138.2 mg/g), HM24 (125.4 mg/g), and HM12 (113.8 mg/g). Advanced equilibrium modeling revealed steric and energetic parameters governing the adsorption mechanism, with HM36 exhibiting the highest density of active sites (Nm = 67.9 mg/g). Each active site accommodated up to three As(V) ions, emphasizing the significance of multi-ionic interactions and vertical stacking at the adsorption interface. The adsorption energy, evaluated using both classic models (< 4 kJ/mol) and advanced statistical physics models (< 9 kJ/mol), confirmed a predominantly physical and exothermic adsorption mechanism. Thermodynamic evaluations further supported the spontaneous and favorable nature of As(V) adsorption across all modified hematite derivatives. The ease of synthesis, low-cost natural precursor, improved adsorption efficiency, and recyclability highlight the potential application of these hematite nanorods in real-world wastewater remediation. The findings suggest that HM36 is a highly efficient and scalable adsorbent for arsenic removal, offering sustainable solutions for industrial and agricultural wastewater treatment.

Keywords Laterite, Hematite, Nano-rods, Adsorption, Pollutants, Advanced equilibrium

[1]Environmental Science and Industrial Development Department, Faculty of Postgraduate Studies for Advanced Sciences, Beni-Suef University, Beni Suef, Egypt. [2]Renewable Energy Science and Engineering Department, Faculty of Postgraduate Studies for Advanced Sciences, Beni-Suef University, Beni Suef 62511, Egypt. [3]Department of Biology, College of Science, Princess Nourah bint Abdulrahman University, P.O. BOX 84428, 11671 Riyadh, Saudi Arabia. [4]Department of Chemistry, College of Science and Humanities in Al-Kharj, Prince Sattam bin Abdulaziz University, Al-Kharj, Saudi Arabia. [5]Department of Biology, College of Science, Imam Mohammad Ibn Saud Islamic University, 11623 Riyadh, Saudi Arabia. [6]Materials Electrochemistry Laboratory, School of Materials Science and Engineering, Yeungnam University, Gyeongsan 38541, Republic of Korea. [7]Materials Technologies and their Applications Lab, Geology Department, Faculty of Science, Beni-Suef University, Beni Suef, Egypt. [8]Applied Science Research Center, Applied Science Private University, Amman, Jordan. ✉email: wailalzoubi@ynu.ac.kr

Chemical contamination of fresh water supplies and its resulting detrimental impacts on humans and the ecosystem are significant issues that pose a grave threat to long-term human safety[1]. The unregulated and frequent release of highly contaminated effluents through mining, agriculture, and industrial operations comprises the main drivers of water contaminants, along with the consequent detrimental environmental impacts. The presence of toxic metals throughout aquatic ecosystems, either as water-soluble ions or in chemical-based complexes, poses a significant risk to the ecosystem and human well-being[2,3]. These elements are characterized as very hazardous, poisonous, non-biodegradable, and malignant ions that tend to accumulate inside the organs for both humans and animals[3–5]. The mining industry, chemical factories, and nuclear fuel generation emit substantial amounts of toxic metallic ions, such as cadmium, arsenic, zinc, barium, mercury, cobalt, lead, and strontium[6–8].

The arsenic ions (As) as water soluble ions have been identified as extremely toxic and carcinogenic water pollutants in the water supplies[9,10]. The advisable concentration of As (V) within drinking water must be kept less than 10 µg/L. Beyond this threshold concentration the arsenic ions poses considerable cancerous risks to the kidneys, skin, lungs, and urine bladder[10,11]. Furthermore, numerous illnesses, including esophageal disorders, cardiovascular illness, gastrointestinal discomfort, hematochezia, emesis, and diabetes, have been identified as consequences of As (V) contaminants[12,13]. An extensive investigation has demonstrated that advanced oxidation, ozonation, adsorption, flocculation, nano-filtration, biological degradation, membrane separation, exchange of ions, and coagulation are successful methods for eliminating various pollutants[6,14,15]. Adsorption stands out as a highly effective and widely adopted technique for water purification, surpassing many conventional decontamination methods in terms of efficiency, cost-effectiveness, and environmental sustainability[12,16,17]. While other techniques, have demonstrated success in pollutant removal, they often suffer from drawbacks including high operational costs, energy-intensive processes, complex maintenance requirements, and secondary waste generationed approaches.

Several studies have proven that adsorption by newly developed materials is a low-cost, efficient, reliable, simple, accessible, and recyclable technique for getting rid of various types of water pollutants[18,19]. A number of criteria, including fabrication prices, production methods, precursor accessibility, adsorption effectiveness, recycling potential, uptake speed, environmental sustainability, uptake selectivity, security, and reactivity, influence the selectivity of an appropriate adsorbing material[16,20]. Consequently, researchers have conducted a comprehensive assessment to develop new adsorbents using readily available and marketable components commonly found in earth's resources[1,21,22]. Researchers highly encourage the application of widely recognized adsorbents derived from earth's materials, including rocks and minerals, due to their tremendous environmental and financial advantages[23]. Iron oxide nanoparticles have specific features that distinguish them from other metallic-based nanostructures[24]. These properties comprise excellent reactivity, adsorption efficiency, visible light absorption effectiveness, significant chemical and mechanical stability, high biocompatibility, and excellent surface area, as well as affordability and wide availability throughout the Earth's resources. Moreover, they exhibit strong conductivity, unique magnetic characteristics, and effortless extraction and recovery[24–26]. These characteristics proved their value in several fields, particularly soil remediation, fertilizer generation, adsorption, medical applications, advanced oxidation, and anti-virus agents[25,27]. Hematite (α-Fe_2O_3) is a very stable iron oxide derivative with n-type semiconductor properties. Hematite has been thoroughly investigated as an essential component in numerous industrial and environmental applications, either as a catalyst or as an adsorbent[24,28]. A variety of parameters, including the fabrication methods, morphological features, raw materials, and precipitating chemicals, significantly influence the physicochemical, textural, and structural qualities of iron oxides[29].

The morphology and structural properties of metal oxide-based nanomaterials extensively affect both adsorption and catalytic effectiveness; therefore, the morphological alterations can drastically boost these characteristics[30]. Earlier studies demonstrate that hematite nanomaterials with modified morphologies, including nanosheets, nanorods, nanospheres, and cauliflowers, possess better physical and chemical characteristics[28]. One-dimensional nanorods have garnered considerable interest due to their consistent geometry, distinctive framework, and exceptional technical properties across several applications[31,32]. Unfortunately, most of the reported methods for producing one-dimensional (1-D) hematite involve incorporation of chemicals as precursor of iron, high formation temperatures, in addition to the expensive cost of the integrated chemicals as surfactants. As a result, it is essential to employ simple and affordable methods at reasonable temperatures, using readily available raw materials. The hydrothermal method has attracted significant interest for its capacity to meticulously control the morphology, microstructure, crystallite dimensions, and physicochemical characteristics of nanomaterials[31,33]. Generally, the morphological transformation of hematite particles by alkaline hydrothermal techniques involved a recrystallization process followed by a ripening process. The two processes are commonly associated with changes in the exposed crystal facets and the growth directions and, in turn, the external morphologies[34]. Furthermore, distinct ionic arrangements in in terms of the changes in the exposed crystalline facets strongly correlate with the reactive properties of hematite nanomaterials, leading to variations in Fe–O bonding topologies, active site quantities, and surface charge properties[24,35].

In this study, a novel hematite-based nano-adsorbent was developed through a simple and eco-friendly hydrothermal modification of lateritic iron ore, transforming it into highly reactive nanorods with enhanced adsorption performance. Unlike conventional iron oxide adsorbents, the synthesized hematite nanorods exhibit superior arsenic uptake due to their increased surface area, controlled crystallographic facets, and improved diffusion pathways. This study not only addresses key limitations in traditional adsorbents but also provides an in-depth evaluation of the adsorption mechanism by integrating steric and energetic modeling approaches, offering valuable insights into ion-adsorbent interactions. Additionally, utilizing low-cost, naturally occurring lateritic iron ore as a precursor not only ensures economic feasibility but also promotes environmental sustainability by repurposing geological resources for water purification. By bridging the gap between material science, surface chemistry, and environmental engineering, this study offers a transformative strategy for arsenic remediation, reinforcing the potential of morphology-controlled nanostructures for scalable and effective water treatment applications.

Experimental work

Materials

Natural iron precursor was delivered as lateritic iron ore from El-Gedida area, Bahariya Oasis, Western Desert, Egypt. The sample chemically composed of 96.73% Fe_2O_3 as the main content in addition to other impurities represented essentially by 1.64% SiO_2 and 0.72% Al_2O_3. NaOH with a purity of over 98% was purchased from Sigma-Aldrich in Egypt. Standard solution of arsenic (V) (1000 mg/L; Sigma-Aldrich) was used during the preparation of the polluted aqueous solutions.

Synthesis of hematite nano-rods

The raw iron ore was crushed and ground by ball mill for 4 h obtaining fine powder with size range from 25 to 60 µm. Certain weights of the ground products (15 g) were pulverized separately within alkaline solution of NaOH (100 mL; 0.4 M) as four experiments under continuous stirring for 2 h at room temperature. After that, the mixtures were transferred into hydrothermal synthesis reactor of Teflon lined stainless steel autoclaves and then treated thermally for different time intervals range from 12 h up to 48 h (12, 24, 36, and 48 h) at 100 °C using electrical and digital muffle furnace with temperature elevation rate 5 °C per min. After this stage, the autoclaves were cool down to the room temperature and the hydrothermally treated particles were extracted by centrifugation for 15 min at rotation speed of 300 rpm. Then, the products were washed, rinsed, and dried for 5 h at 80 °C. The dried products were labeled as HM12, HM24, HM36, and HM48 for the modified hematite products for 12 h, 24 h, 36 h, and 48 h, respectively and kept for the further characterization and applications steps (Fig. 1).

Characterization instruments

The mineral phases and crystallographic properties were examined and explored by utilizing X-ray diffraction (XRD) patterns produced by the PANalytical-Empyrean X-ray diffractometer. The range of values for the 2 Theta angles determined with the diffractometer is between 0 and 70°. A Fourier transform infrared spectrometer (FTIR-8400S; Shimadzu) that possesses a 400–4000 cm^{-1} determining range was employed in addition to the energy dispersive X-ray (EDX) investigation of elemental contents to establish the changes in the functioning chemical groups across the production processes. The exterior properties of the produced structures were studied by applying a Gemini Zeiss Ultra 55 scanning electron microscope. Before examination, the outer surfaces of the products under exploration had been coated with a thin film of gold through the spraying process. To evaluate the textural properties of the synthesized hematite-based nanorods, the Brunauer–Emmett–Teller (BET) method was employed for surface area determination, while the Barrett–Joyner–Halenda (BJH) model was used to analyze pore size distribution. Nitrogen adsorption–desorption isotherms were recorded at 77 K using a Micromeritics ASAP 2020 surface area analyzer. Prior to analysis, the samples were degassed under vacuum at 120 °C for 12 h to remove any adsorbed moisture or contaminants.

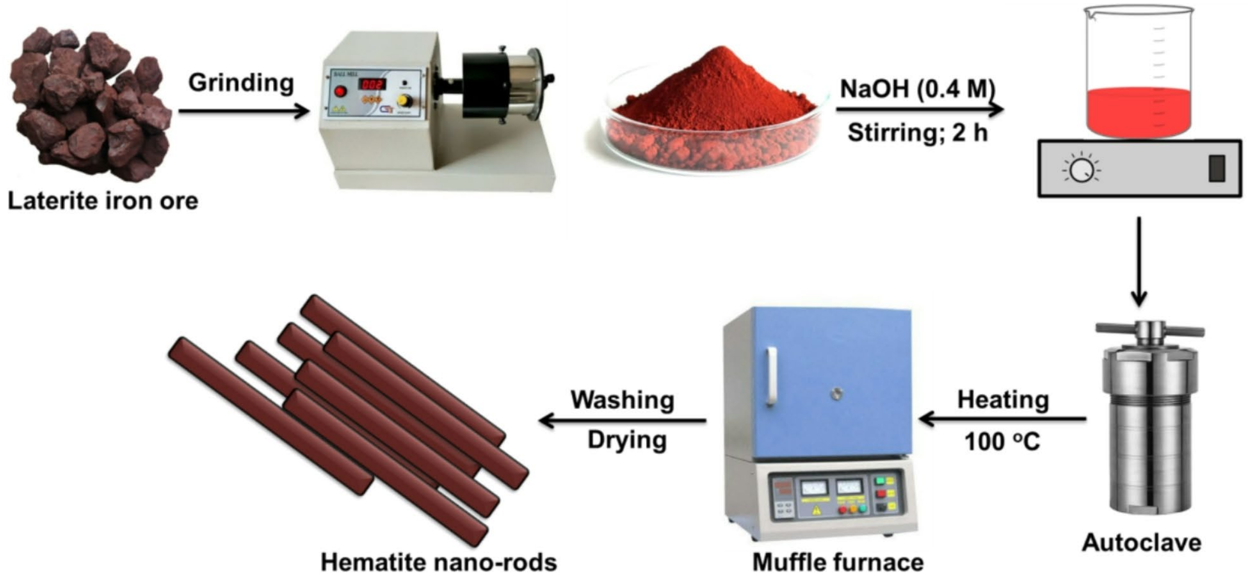

Fig. 1. Schematic *diagram* for the synthesis procedures of hematite nano-rods from lateritic iron ore.

Adsorption studies

Experimental adsorption studies of As (V) were conducted in batches. The experimental parameters that were evaluated were the following: pH (pH 2–8), time span of the reaction (30–480 min), amount of modified hematite derivatives (0.2 g/L), and dissolved contents of the tested pollutants (25–300 mg/L) under three different operational temperature values (20 °C, 30 °C, and 40 °C) and particular volumes (100 mL). The mixing and homogenization during the adsorption tests was conducted using orbital shaker. Three rounds were conducted for each test, and the averages of the obtained findings were consistently used in the calculations, with standard deviations below 4.6%. The achieved uptake capacities (Q_e) of As (V) using HM12, HM24, HM36, and HM48 were calculated employing Eq. 1 considering the values of starting concentration (C_o), remaining concentration (C_e), treated volume (V), and adsorbent mass (m). The remaining As (V) ions were quantitatively determined using inductively coupled plasma mass spectrometry (Perkin Elmer). The arsenic (V) standards used in the calibration processes were acquired by Merck Company (Germany) and subsequently approved by the National Institute of Standards and Technology (NIST).

$$\mathrm{Q_e}\ (\mathrm{mg/g}) = \frac{(\mathrm{C_o} - \mathrm{C_e})\mathrm{V}}{\mathrm{m}}[22] \tag{1}$$

Conventional and modern equilibrium investigations

The adsorption of As (V) using HM12, HM24, HM36, and HM48 has been described using well-established traditional kinetics, classic equilibrium, and updated isotherm investigations in accordance with the theoretical statistical physics hypothesis (Table S1). The kinetic and conventional isotherm modeling have been assessed employing the non-linear fitting levels of the retention data of As (V). The evaluation implemented the parameters of the coefficient (R^2) (Eq. 2) and Chi-squared (χ^2) (Eq. 3)[36]. The nonlinear fitting qualities with the modern isotherm models' descriptive equations and the remediation results of SFR and PO_4^{3-} have been examined using the determination coefficient (R^2) and root mean square error (RMSE) (Eq. 4)[36]. The variables m′, p, Qe_{cal}, and Qe_{exp} in the equation correspond to the outcomes of As (V) adsorption by HM12, HM24, HM36, and HM48, parameters affecting the uptake reaction, predicted capacities of ions adsorption, and determined capacities of ions adsorption, respectively.

$$\mathrm{R}^2 = 1 - \frac{\sum(Q_{e,exp} - Q_{e,cal})^2}{\sum(Q_{e,exp} - Q_{e,mean})^2} \tag{2}$$

$$\chi^2 = \sum \frac{(Q_{e,exp} - Q_{e,cal})^2}{\mathrm{Q_{e,\ cal}}} \tag{3}$$

$$\mathrm{RMSE} = \sqrt{\frac{\sum_{i=1}^{m}(\mathrm{Qe_{cal}} - \mathrm{Qe_{exp}})^2}{\mathrm{m}' - \mathrm{p}}} \tag{4}$$

Results and discussion

Characterization of the adsorbent

XRD analysis

The crystalline structure of both unprocessed iron oxide and its modified form was evaluated according to their XRD patterns (Fig. 2). The analyzed pattern of the untreated material indicates its composition as α-hematite, which exhibits a distinctive rhombohedral crystal structure (JCPS Cd. No. 33-0664; ICDD No. 01-079-0007). The diffraction peaks have been detected at 24.5° (012), 33.5° (104), 35.9° (110), 41.2° (113), 49.7° (024), 54.5° (116), 62.7° (214), and 64.3° (300) (Fig. 2A) (JCPS Cd. No. 33-0664). Subsequent to the alteration procedures, the resultant patterns of HM12, HM24, HM36, and HM48 reveal no alterations in the detected hematite phase; however, they present significant evidence about the influence of the treatment steps on the structural characteristics of the material being studied (Fig. 2B–E). The peaks showed an obvious decline in their intensities, and several peaks were difficult to identify, along with a significant shift to lower positions. The principal peaks of hematite observed during the HM12 examination were shifted to 24.2°, 33.2°, 35.7°, 40.9°, 49.4°, 54.4°, 62.3°, and 64.2° (Fig. 2B). The HM24 sample exhibited deviations to 24.05°, 33.17°, 35.6°, 40.8°, 49.3°, 54.2°, 62.3°, and 63.8° (Fig. 2C).

Generally, the degree of deviations and the reduction in the intensities of the essential peaks increase significantly as the modification periods increase from 12 to 48 h. These demonstrated either a reduction in the crystallite size or strong lattice deformation. Nevertheless, hematite crystals with completely different exposed facets exhibit changes in their peak strengths. In the modified forms (HM12, HM24, HM36, and HM48), there is a noticeable reduction in the intensities of (110) and (104), the main peaks, compared to the original sample. These observations indicate that the modified crystals have different exposed faces[24,35]. Also, the calculated average crystallite size demonstrates such structural impact, as the size was reduced from 18 nm for the raw sample to 15.6 nm, 15.2 nm, 13 nm, and 12.4 nm for HM12, HM24, HM36, and HM48, respectively.

FT-IR analysis

The analyzed FT-IR spectra provide significant evidence of structural alterations after the alkaline treatment of starting iron oxide (Fig. 3). The spectrum of the unprocessed mineral reveals no evidence of OH groups, whether associated with adsorbed water molecules or the structural OH of iron hydroxide complexes. The identified bands at 428 cm^{-1} (Fe–O-Fe) and 525 cm^{-1} (Fe–O) demonstrated the presence of the hematite phase

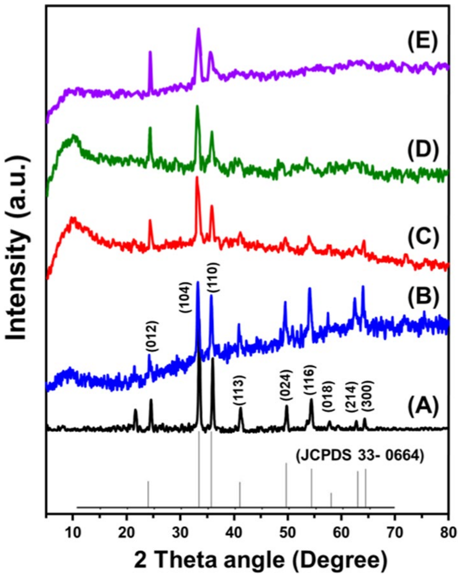

Fig. 2. XRD patterns of raw *lateritic* iron ore (**A**) and modified hematite forms by alkaline modification for different periods (HM12 (**B**), HM24 (**C**), HM36 (**D**), and HM48 (**E**)).

(Fe_2O_3) (Fig. 3A)[37,38]. The prominent band around 889 cm^{-1} (Fe–O) may indicate the presence of goethite as an admixed phase of minor content[39]. The observable bands at 798 cm^{-1} and 1005 cm^{-1} indicated the presence of Si(Al)-O groups, which match the existing silicate or clay impurities (Fig. 3A)[37,40]. The influence of the alkaline treatment procedure was markedly discernible in the analyzed FT-IR spectra of HM12, HM24, HM36, and HM48. The spectra indicated the presence of many additional bands associated with hydroxyl groups (around about 3400 cm^{-1}, 3000 cm^{-1}, and 1630 cm^{-1}) (Fig. 3B–E)[38]. This illustrates the hydration impact of the treatment processes and alterations in the exposed crystallographic facets. Furthermore, the corresponding bands of the iron-bearing chemical groups exhibited a significant increase in both intensity and width, along with a notable displacement from their initial positions. The recognition of the bands of hematite (Fe–O-Fe and Fe–O) shifted to higher locations. This indicated the structural influence of the modification procedure on the hematite crystallographic structure.

SEM analysis

The modification step also affected significantly the morphological features of the hematite grains (Fig. 4). The SEM images of the inspected hematite grains within the used lateritic iron ore appeared as massive and agglomerated particles that sometimes appeared with irregular topography (Fig. 4A). This irregular topography can be described as a coating layer of nanograins that possesses flakey, longitudinal, and elliptical shapes (Fig. 4B). By conducting the alkaline modification steps, the SEM images revealed the significant morphological transformation of the modified hematite into well-developed nanorods. All the modified samples for different periods (HM12 (Fig. 4C), HM24 (Fig. 4D,E), HM36 (Fig. 4F,G), and HM48 (Fig. 4H,I)) exhibit these characteristics. However, the inspected images reveal that extending the modification periods from 12 h (HM12) to 36 h (HM36) enhanced the development of the rods. The investigated HM12 and HM24 samples demonstrate the existence of relict fractions corresponding to the starting lateritic iron ore, reflecting non-complete conversion of these particles into nanorods. The SEM images of the 48-h-treated sample (HM48) showed significant distortion in the rods that were detected in the SEM images of the HM36 sample. Also, there was detection of considerable changes for the rod-like grain to flake or irregular grains after conduction of the modification step for 48 h. Such morphological features can have a significant impact on the hematite's surface area, reactivity, and exposed active sites, as well as its adsorption performance.

Brunauer–Emmett–Telle analysis

The textural properties of synthesized HM12, HM24, HM36, and HM48 particles were evaluated based on their nitrogen adsorptiopn/desorption isotherm curve (Fig. 5). The recognized curves can be classified as a type IV isotherm according to the basics of the International Union of Pure and Applied Chemistry (IUPAC). Additionally, in contrast to the dectced curve for HM12 (Fig. 5A), the plotted curves of HM24 (Fig. 5B), HM36 (Fig. 5C), and HM48 (Fig. 5D) exhibit noticeable hysteresis loops of type H3[41]. Such criteria reflect the existence of nanopores (mesopores (2 to 50 nm)) within the structure of HM24, HM36, and HM48, which can be assigned to the non-rigid aggregation or slit-shaped pores[41]. The estimated average pore dimaters of HM12, HM24, HM36, and HM48 are 4.48 nm, 4.5 nm, 3.6 nm, and 4.2 nm, respectively. The measured surface area significantly improved as the treatment periods increased from 12 to 36 h, but then declined again when the period was extended to 48 h. This is in agreement with the recognized morphological features based on the SEM images. The measured surface area values of HM12, HM24, HM36, and HM48 are 83.5 m^2/g, 141.5 m^2/g,

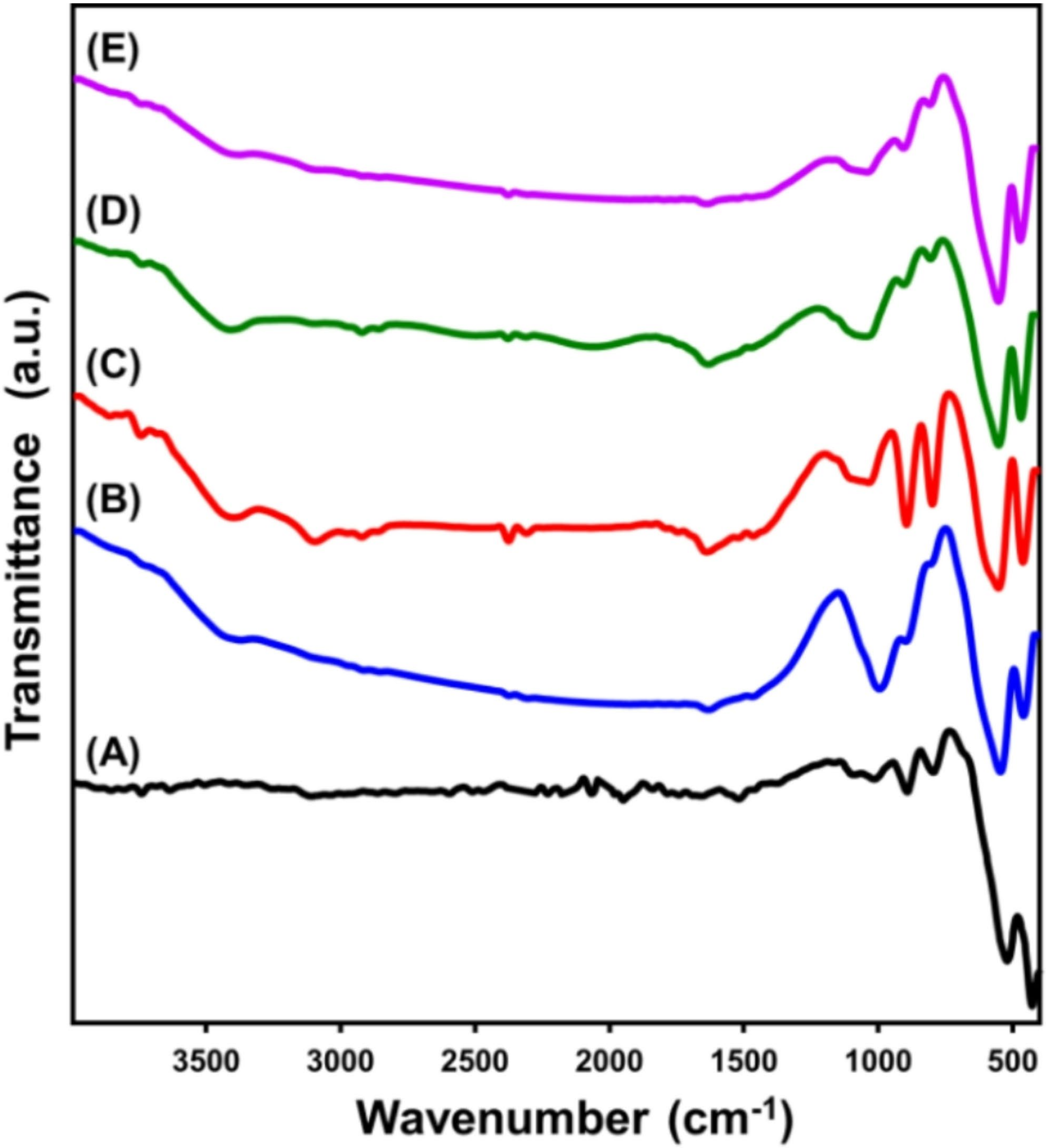

Fig. 3. FT-IR spectra of *raw* lateritic iron ore (**A**) and modified hematite forms by alkaline modification for different periods (HM12 (**B**), HM24 (**C**), HM36 (**D**), and HM48 (**E**)).

154.7 m^2/g, and 144.6 m^2/g, respectively. The textural properties of the synthetic strucrures, specifically HM24, HM36, and HM48, enable their effective application as adsorbents for water contaminants or as heterogeneous catalysts. They can also serve as drug delivery systems or catalyst supports due to their porosity and significant surface area.

Adsorption results

Effect of pH

The pH of the aqueous solution has a significant impact on the essential surface charges and ionizing characteristics of water-soluble chemicals[42]. The experimental pH effects were detected throughout a range of pH levels ranging from 2.0 to 8.0. The other variables were held constant: a reaction time of 90 min, a temperature of about 20 °C, a volume of 100 mL, an As (V) concentration of 100 mg/L, and an HM dosage of 0.2 g/L. The adsorption of As

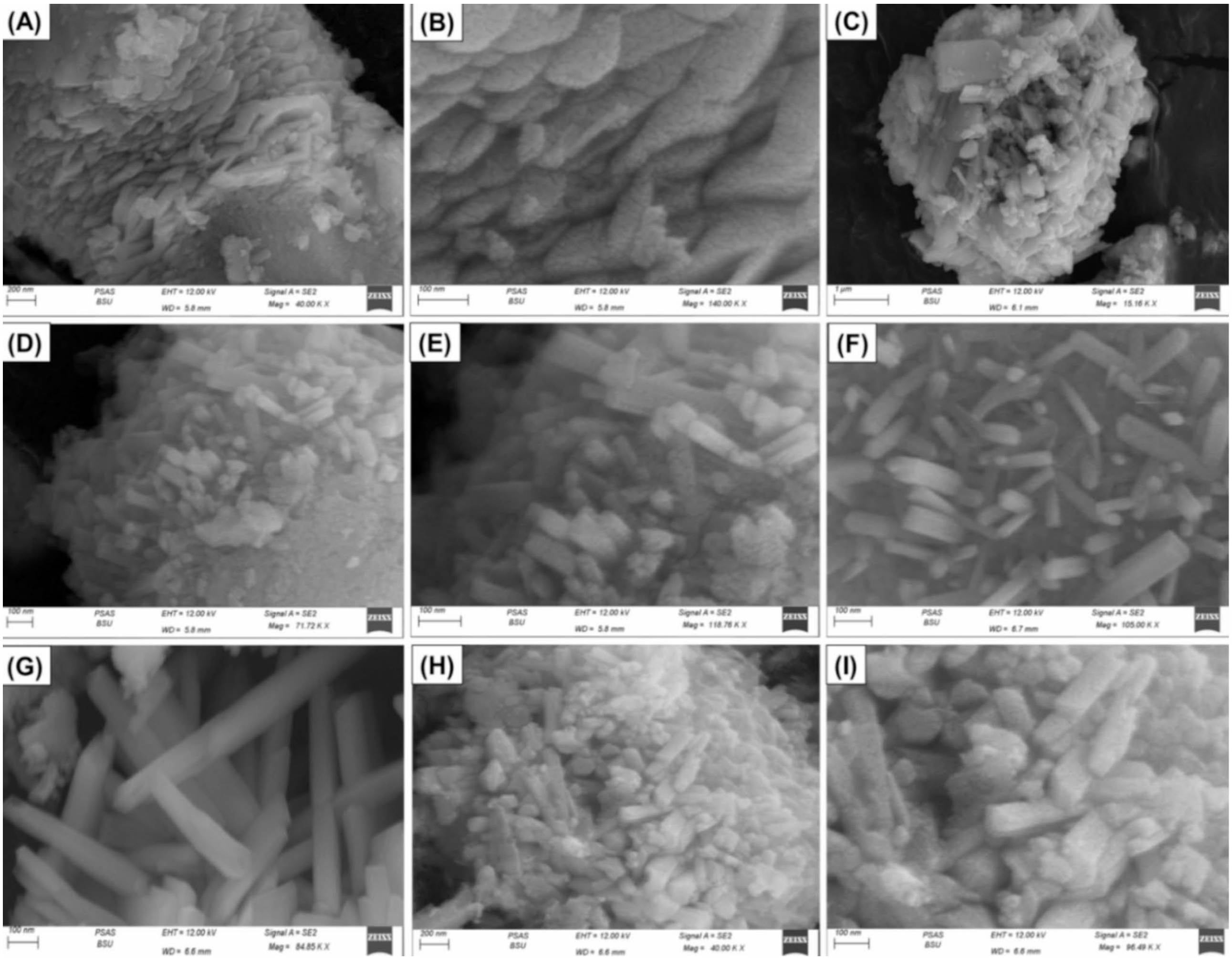

Fig. 4. SEM images of lateritic iron ore (**A**,**B**), *modified* HM12 product (**C**), modified HM24 product (**D**,**E**), modified HM36 product (**F**,**G**), and modified HM48 product (**H**,**I**).

(V) demonstrates a significant rise with higher pH values up to a pH of 6.0 for the four tested forms of hematite (HM12 (50.3 mg/g), HM24 (58.2 mg/g), HM36 (73.4 mg/g), and HM48 (62.3 mg/g)) (Fig. 6). The pH levels above 6.0 revealed a significant decrease in the uptake efficiency of As (V) ions by HM12, HM24, HM36, and HM48 (Fig. 6). The reported behavior can be explained by the ionizing or speciation characteristics of As (V) as water-soluble ions under various pH conditions, as well as the impact of pH values on the predominant surface charges at the interfaces of the modified hematite varieties under study. At various pH levels, the speciation of As (V) significantly influences the described adsorption characteristics. The neutral version of As (V) (H_3AsO_4) is detectable from pH 2.0 up to pH 4.0, whereas the acidic types, including $HAsO_4^{2-}$ and AsO_4^{3-}, are identified as the most common species from pH 7.0 until pH 12.0[12,43,44]. The acidic types of As (V) at elevated pH settings exhibit significant repulsive characteristics away from the exterior chemical groups of HM12, HM24, HM36, and HM48, which are influenced by deprotonation effects, resulting in more negative charges.

Therefore, HM12, HM24, HM36, and HM48 encourage the adsorption of As (V) at pH 6.0 by maintaining substantial amounts of positively charged groups on their surfaces, which facilitates efficient electrostatic interactions with the acidic types of As (V) ions[44], which become saturated with hydroxyl ions. Consequently, the adsorption of As (V) by HM12, HM24, HM36, and HM48 at pH 6.0 is encouraged as it maintains substantial amounts of positively charged groups onto the adsorbent's surfaces, facilitating efficient electrostatic interactions with the acidic types of As (V) ions[45]. Inspections of pH levels at zero charge ($pH_{(pzc)}$) were consistent with previous results. The determined pH pzc were 7.3 (HM12), 7.3 (HM24), 7.5 (HM36), and 7.6 (HM48) (Fig. S1). Under these pH levels, the exterior charges are primarily positive, leading to considerable electrostatic attraction of As (V) ions towards the interfaces of the modified hematite-based adsorbents[46–48].

Contact time

An analysis was conducted to assess the adsorption characteristics of HM12, HM24, HM36, and HM48 with regard to the efficacy of eliminating As (V). The examination encompasses a testing range from 30 to 480 min. After verifying the levels of essential parameters, including As (V) content (100 mg/L), temperature (20 °C),

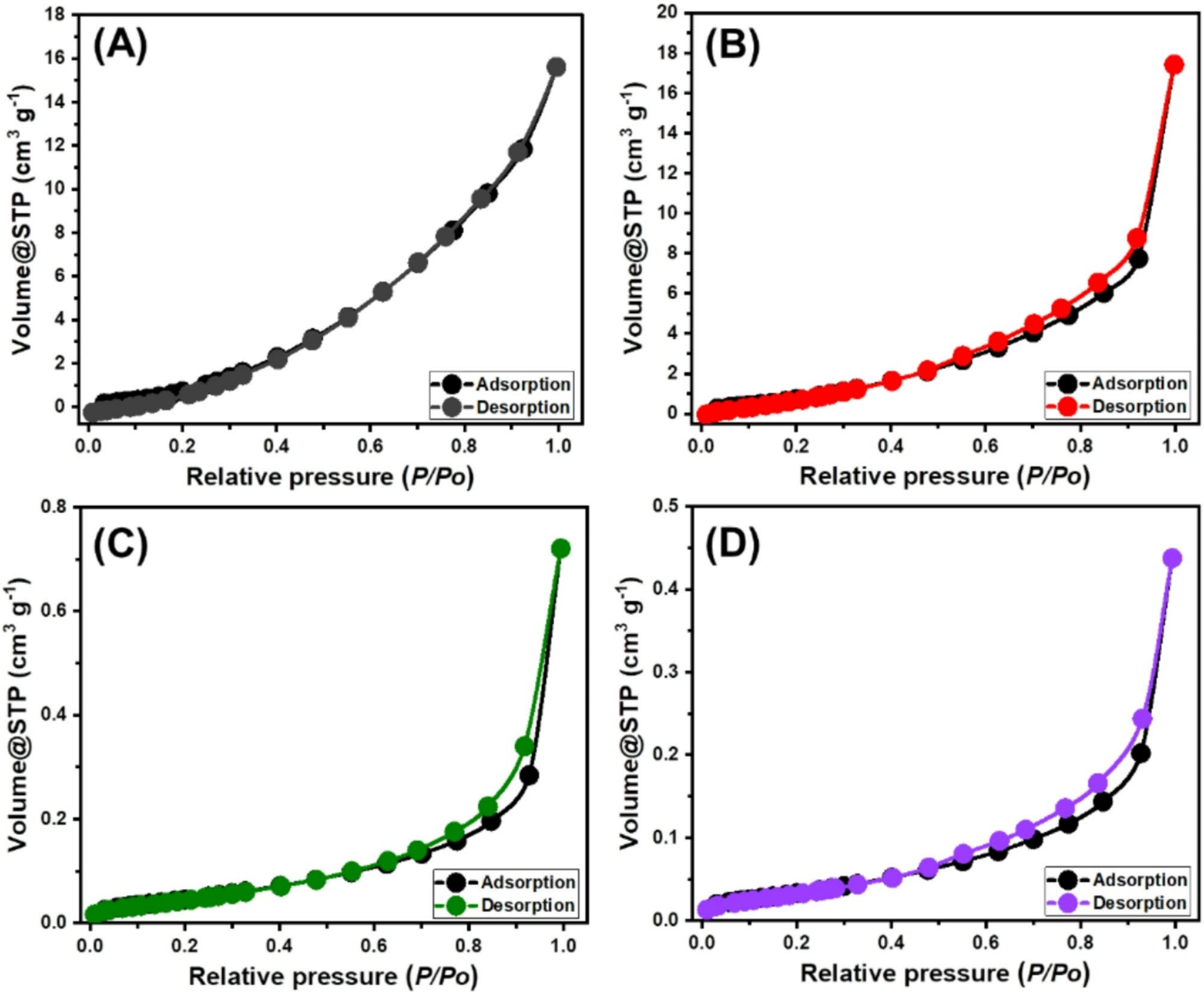

Fig. 5. The nitrogen adsorption/desorption isotherm curves of the *hematite* modified derivatives including HM12 (**A**), HM24 (**B**), HM36 (**C**), and HM48 (**D**).

volume (100 mL), pH (6), and quantity (0.2 g/L) at fixed values, we evaluated the specific impact of distinct time periods. All over the experiments, the effectiveness of HM12, HM24, HM36, and HM48 in removing As (V) ions showed a significant increase in both the quantity of ions adsorbed and their experimental uptake rates. Moreover, it is crucial to acknowledge that the time frame of the experiments significantly influences the detectable enhancements in the recognized uptake properties, attaining about 240 min (Fig. 7A). Nevertheless, there were no notable changes or improvements seen in the rate of elimination of As (V) ions or the amount of these ions adsorbed after the stated contact durations. Previous findings suggest that HM12, HM24, HM36, and HM48 can serve as adsorbents for As (V) ions, reaching their maximum stability after a specific duration of 240 min. Under such equilibration conditions, the adsorption qualities of HM12, HM24, HM36, and HM48 were measured to be 91.4 mg/g, 98.7 mg/g, 119.4 mg/g, and 112.5 mg/g, respectively (Fig. 7A). In the early phases of the evaluation, substantial improvements in the adsorption rates of As (V) ions using the four modified hematite-based adsorbents were observed, along with larger amounts of adsorbed ions. The detected improvements were ascribed to the extensive presence of both active and free sites throughout the surfaces of their particles[49]. With the extension of the examination's time, the number of unoccupied sites decreased significantly as the examination's time was extended. The prolonged adsorption of As (V) ions, which consumes the previously described sites and reduces the overall number of unoccupied sites, is the primary factor contributing to this response. Consequently, there was a drastic decrease in the rates by which the As (V) ions adsorbed after certain durations. Furthermore, the use of HM12, HM24, HM36, and HM48 resulted in modest enhancement or consistent characteristics in As (V) adsorption, indicating a state of equilibrium. By completely filling all of the existing active functional sites and preventing further adsorption of As (V) on their exteriors, the hematite-based adsorbents attend their equilibrium phases[50].

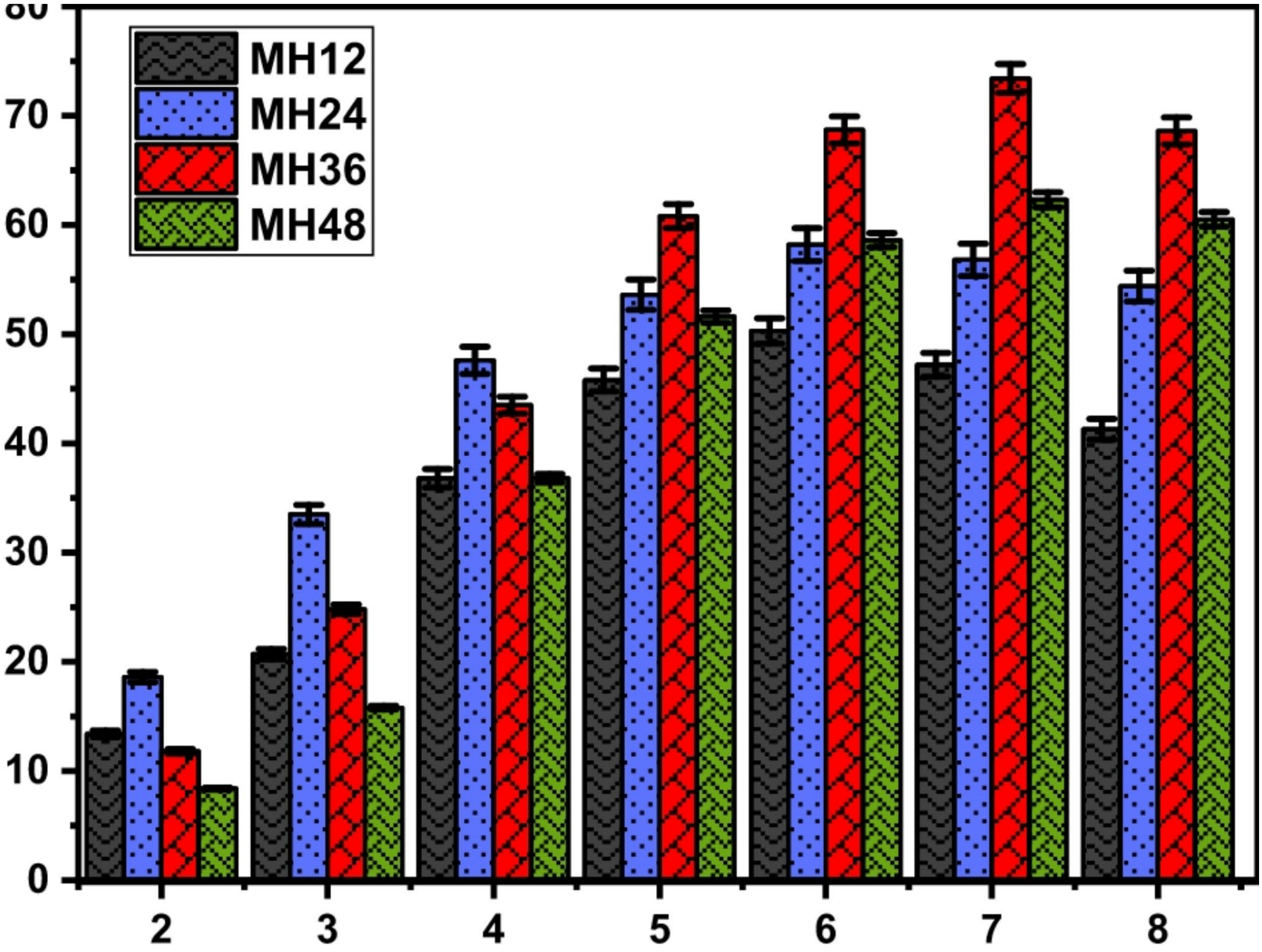

Fig. 6. The experimental effect of the solutions pH on the uptake behaviors of As (V) by HM12, HM24, HM36, and HM48.

Intra-particle diffusion behavior

The examination of intra-particle diffusion characteristics may be used to illustrate the mechanistic stages and adsorption characteristics of As (V) ions employing HM12, HM24, HM36, and HM48. Figure 7B displays three distinct sections of the presented curves, each with different slopes. The analyzed curves exhibit spatial displacements relative to their initial positions, indicating the simultaneous presence of multiple adsorption mechanisms in addition to the diffusion mode of As (V) ions[6,51]. The processes generally consist of three main phases: (1) interactions between dissolved ions and the unbound uptake sites distributed across the outer surfaces of modified hematite-based adsorbents (boundary or external adsorption); (2) the layered adsorption processes (internal adsorption) in conjunction with the diffusion properties of the dissolved chemicals; and (3) the influence of equilibrium or saturating situations[52]. The study's early findings show that the external uptake mechanisms are the main ones that bind As (V) ions to the surfaces of HM12, HM24, HM36, and HM48. These were the most important pathways that were consistently found at all stages of the adsorption activities (Fig. 7B). During this stage, the effectiveness of adsorbing As (V) ions depends on the total number of sites located across the interfaces of modified hematite-based adsorbents. The efficacy of further layered or internal adsorption methods was immediately confirmed by increasing the duration until all exterior sites were completely occupied (Fig. 7B)[46,52]. Moreover, this step incorporates the effects of As (V) ion diffusion mechanisms. Once equilibrium conditions are established, the final processes of As (V) adsorption via HM12, HM24, HM36, and HM48 significantly influence the process. These findings show that As (V) ions, successfully adsorbed, occupied all available sites[53,54]. Throughout this phase, molecular and interionic attraction processes expedite the elimination of As (V) ions[45].

Kinetic modeling

In order to investigate the time-dependent impacts and comprehend physical mechanisms such as mass transfer pathways as well as chemical-based pathways that regulate absorption efficacy, it is imperative to model the kinetics of the uptake reactions[55]. The kinetics of As (V) ions removal activities were analyzed employing conventional pseudo-first-order (P.F.) and pseudo-second-order (P.S.) numerical models. The P.F. model was used to elucidate the correlation between the rates at which the As (V) ions completely occupy the interaction binding

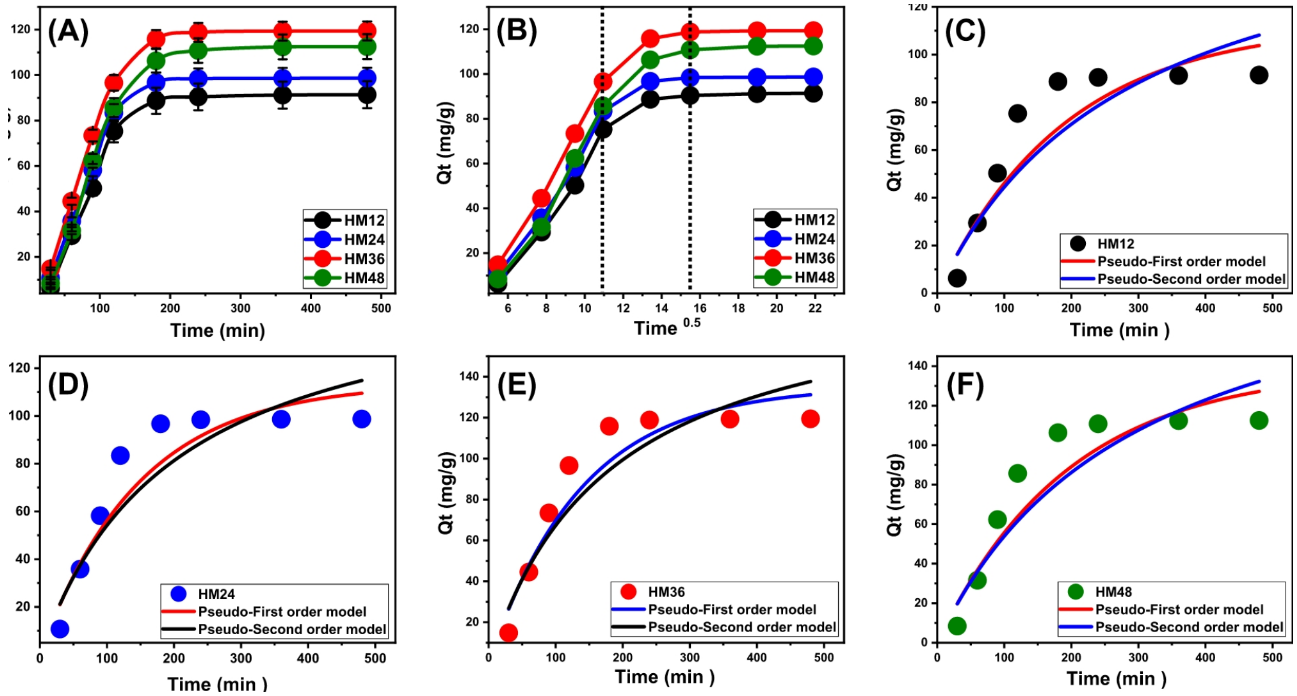

Fig. 7. The experimental effect of the contact time on the uptake behaviors of As (V) by the modified hematite based adsorbents (**A**), the intra-particle diffusion curves of the adsorption processes (**B**), and fitting of the As (V) uptake behaviors with the kinetic models (**C** (HM12), **D** (HM24), **E** (HM36), and **F** (HM48)).

	Kinetic models				
Models	**Parameters**	**HM12**	**HM24**	**HM36**	**HM48**
Pseudo-First-order	K$_1$ (min^{-1}(	0.0052	0.0068	0.0073	0.0051
	Qe $_{(Cal)}$ (mg/g)	112.9	113.9	135.3	121.4
	R^2	0.89	0.92	0.93	0.90
	X^2	5.3	3.4	3.02	5.4
Pseudo-second-order	k$_2$ (g mg^{-1} min^{-1})	1.99×10^{-5}	3.06×10^{-5}	2.89×10^{-5}	1.57×10^{-5}
	Qe $_{(Cal)}$ (mg/g)	173.5	162.9	189.9	214.0
	R^2	0.87	0.89	0.91	0.89
	X^2	5.98	4.2	4.4	6.2

Table 1. The mathematical parameters of the evaluated kinetic models.

sites, in addition to their entire quantities. The P.S. principles may highlight the link between analyzed adsorbent characteristics over a specific period of time. The correlation between the pollutants adsorption tendencies and the inspected two kinetic models has been assessed by implementing nonlinear fitting variables that correspond to their relevant equations. The analysis of correlation coefficients (R^2) and Chi-squared (X^2) values (Table 1; Fig. 7C–F) determined the best levels of fitting. The R^2, in conjunction with the X^2 data, demonstrates that the basic hypotheses of the P.F. model provide a better explanation for the adsorption characteristics of As (V) ions employing all the modified hematite-based adsorbents (HM12 (Fig. 7C), HM24 (Fig. 7D), HM36 (Fig. 7E), and HM48 (Fig. 7F)) than the evaluated P.S. concept. The numerical simulation of the P.F. model yielded the predicted quantities of As (V) ions that HM12, HM24, HM36, and HM48 can adsorb, which are 112.9 mg/g, 113.9 mg/g, 135.3 mg/g, and 121.4 mg/g, respectively. These values closely matched the experimentally obtained quantities when compared to the P.S. model's results. The established consistency corroborates the previously acquired findings, which emphasize the better suitability of the P.F. hypothesis regarding the kinetic analyses (Table 1). According to P.F. theoretical terms, the main factors contributing to the adsorption of As (V) ions using the four modified hematite-based adsorbents include physical processes, particularly van der Waals forces and electrostatic attractions[18,56]. The analyzed fitting factors also show significant similarities with the P.S. model; however, the P.F. model achieves a better degree of match. Previous studies have shown that several chemical mechanisms, including hydrogen bonding, complexation, and hydrophobic interactions, are likely to either enhance or have a negligible impact on the adsorption of As (V) ions using HM12, HM24, HM36, and HM48[46,55]. Physical approaches may generate successive uptake layers over the earlier-formed layers of the chemically adsorbed As (V) ions[57].

Initial As (V) concentration

The analysis here investigated the impact of initial As (V) concentrations on the maximum elimination activities as measured by HM12, HM24, HM36, and HM48, together with the corresponding equilibrium conditions, across the evaluated range from 25 to 300 mg/L. The other essential parameters affecting the elimination of As (V) were maintained fixed at certain values, including a total volume equal to 100 mL, a period of 24 h, a dose of 0.2 g/L, and temperatures ranging from 293 to 313 K. A correlation has been found between elevated concentrations of As (V) ions and the detected rise in their adsorbed amounts using HM12, HM24, HM36, and HM48 (Fig. 8A–D). In a specific volume, increasing the concentration of As (V) ions significantly improves soluble chemicals' diffusion, driving forces, and mobility properties. This enhancement augmented the ability to interact with larger amounts of the existing active sites that are easily accessible on the exteriors of HM12, HM24, HM36, and HM48. Therefore, the effectiveness of adsorbing As (V) using HM12, HM24, HM36, and HM48 was significantly improved relative to the tested concentrations[58]. Nevertheless, this correlation can only be observed until specific contents of As (V) ions. Beyond such concentrations, raising the starting levels of As (V) doesn't seem to have a positive impact on their binding performances to the interfaces of HM12, HM24, HM36, and HM48. Determining the equilibrium situations facilitates significantly in determining the highest adsorption

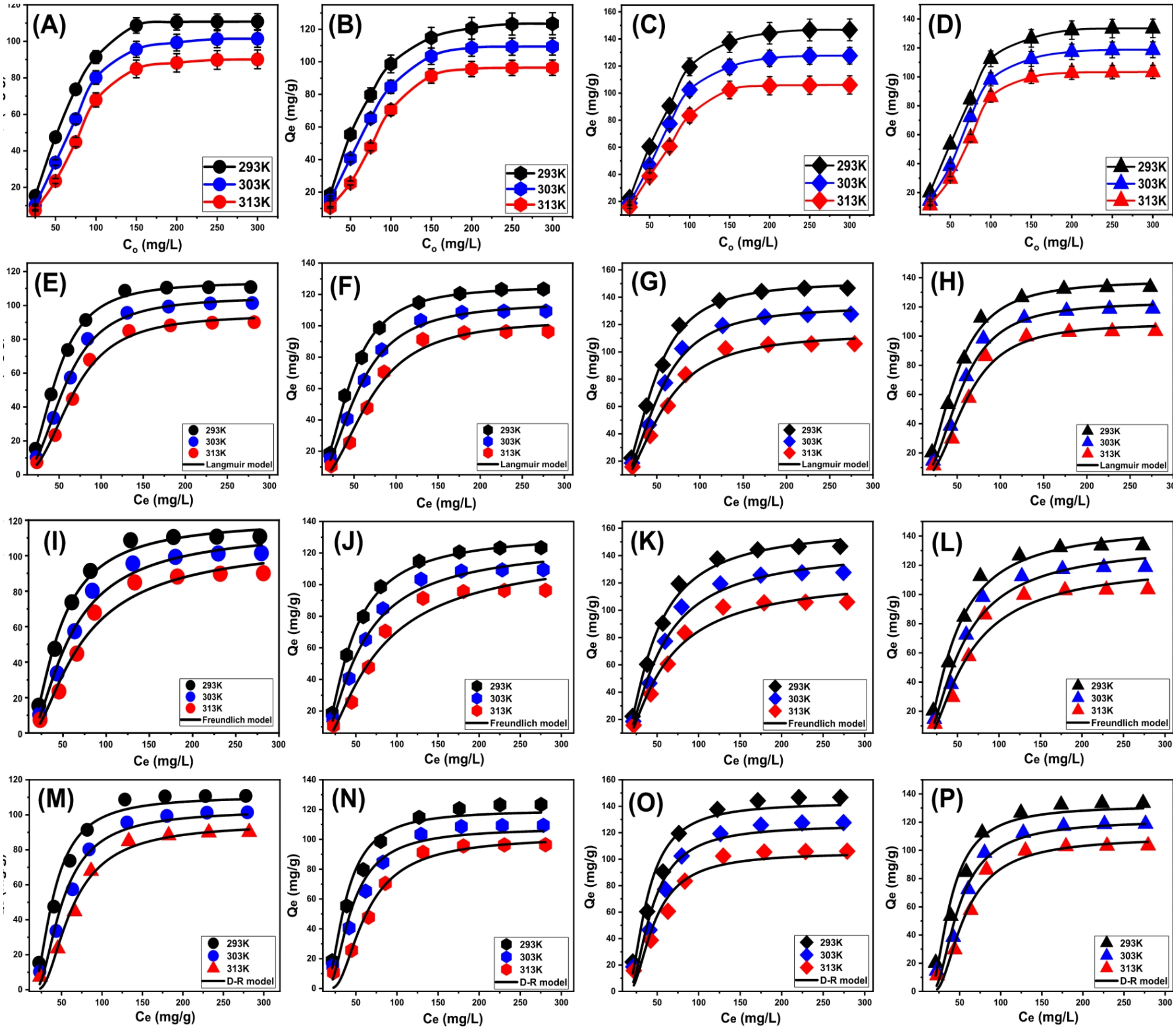

Fig. 8. The experimental effect of starting *concentration* of As (V) on the uptake capacities of modified hematite based adsorbents (**A** (HM12), **B** (HM24), **C** (HM36), and **D** (HM48)), fitting of the uptake results with Langmuir model (**E** (HM12), **F** (HM24), **G** (HM36), and **H** (HM48)), fitting of the uptake results with Freundlich model (**I** (HM12), **J** (HM24), **K** (HM36), and **L** (HM48)), and fitting of the uptake results with D-R model (**M** (HM12), **N** (HM24), **O** (HM36), and **P** (HM48)).

performances of As (V) by the used hematite-based adsorbents. The highest adsorption capacities of As (V) by HM12 were determined to be 110.8 mg/g at a temperature of 293 K, 101.4 mg/g at 303 K, and 90.1 mg/g at 313 K (Fig. 8A). The measured values for HM24 were 123.4 mg/g at 293 K, 109.4 mg/g at 303 K, and 96.4 mg/g at 313 K (Fig. 8B). For HM36, the determined capacities were 146.7 mg/g (293 K), 127.6 mg/g (303 K), and 106 mg/g (313 K) (Fig. 8C), while the recognized values by HM48 were 133.5 mg/g (293 K), 118.7 mg/g (303 K), and 103.4 mg/g (313 K) (Fig. 8D). The observed decrease in As (V) uptake effectiveness using HM12, HM24, HM36, and HM48 at higher temperatures indicates that the reactions under investigation exhibit exothermic characteristics. Furthermore, the HM36 sample outperforms the other investigated products (HM12, HM24, and HM48) in terms of adsorption performance. These results are in agreement with the detected morphological features and the measured surface area, as the sample displayed well-developed nanorods and a better surface area than the other three modified forms.

Classic isotherm models

Traditional equilibrium analyses for the conducted adsorption processes have been performed in order to evaluate the dispersion of water-soluble pollutants throughout the aqueous solutions alongside the incorporated adsorbent at concentrations higher than the equilibrium level. Conventional equilibrium modeling approaches have a significant impact on illustrating the effective mechanisms. The frequently used isotherm functions provide important insights into three factors: (a) the sorbate's selectivity towards the adsorbent's reactive interfaces; (b) the theoretical amount of soluble chemical ions that could potentially interact with these interfaces; and (c) the maximal adsorption capacities. The present investigation analyzes the equilibrium properties of As (V) ions by evaluating their bonding aspects using the Langmuir (Fig. 8E–H), Freundlich (Fig. 8I–L), and Dubinin-Radushkevich (D-R) (Fig. 8M–P) isotherm theories. The degree of alignment between the assumed equilibrium hypotheses stated in the aforementioned models and the measurable adsorption behaviors of As (V) ions was evaluated through non-linear regression methods. The analysis included the examination of the correlation coefficient (R^2) and the Chi-squared (X^2) measurements. The investigation of R^2 and X^2 indicates that the HM12, HM24, HM36, and HM48 particles tend to adsorb the As (V) ions according to Langmuir's hypothesis rather than the Freundlich concept (Table 2). The mentioned equilibrium behavior suggests that As (V) ions display consistent and homogeneous behaviors during their uptake by reacting sites that are distributed on the interfaces of HM12, HM24, HM36, and HM48. As a result, the adsorbed As (V) ions form a single layer or monolayer of their ions on the hematite-based adsorbents' surfaces[18,59]. Furthermore, the analysis showed that HM12, HM24, HM36, and HM48 particulates had favorable adsorption behaviors for As (V) ions, as evidenced by the R_L values that are under 1[51]. The results of the theoretical study showed that HM12 has maximum adsorption capacities ($\mathrm{Q}_{\mathrm{max}}$) of 113.9 mg/g at 293 K, 105 mg/g at 303 K, and 94.6 mg/g at 313 K. The expected values for HM24 are 125.4 mg/g at 293 K, 115.3 mg/g at 303 K, and 104 mg/g at 313 K, whereas the reported values for HM36 are 151.4 mg/g (293 K), 133.5 mg/g (303 K), and 113.6 mg/g (313 K). The expected values for HM48 are 138.2 mg/g (293 K), 123.3 mg/g (303 K), and 108.6 mg/g (313 K) (Table 2).

The equilibrium parameters of the D-R model provide a comprehensive understanding of the energy variations exhibited by HM12, HM24, HM36, and HM48 nanoparticles throughout the removal processes of As (V) ions, irrespective of the particle's levels of heterogeneity or homogeneity. Examining the results of the D-R modeling provides essential details about the Gaussian energy (E) and its significance for understanding the key mechanisms, whether physical or chemical in nature. The uptake mechanisms may be categorized into three separate groups based on their energetic levels: < 8 kJ/mol, from 8 to 16 kJ/mol, and above 16 kJ/mol. At these energy levels, the main mechanisms comprised mostly of prominent physical, weak chemical, and/or complicated interactions between physical and chemical processes and strong chemical activities in order[54]. The observed values of energy (E) for As (V) ions uptake processes using HM12, HM24, HM36, and HM48 were found to be below the set energy limits for the physical processes (less than 8 kJ/mol) (Table 2).

Advanced isotherm models

The use of statistical physics methods to model the equilibrium characteristics of adsorption reactions could provide a comprehensive examination of these processes' distinctive characteristics. The mathematical models used in the present investigations assess the interactions between external reactive chemical groups that function as interacting binding sites throughout the absorbent's interface and water-soluble pollutants. The mathematical equations utilized in this study provide reliable calculated parameters that precisely reflect the main mechanistic processes, encompassing both energetic and steric factors. The steric parameters included in the computations are Nm, which quantifies the total quantity of occupied adsorption sites across the interfaces of HM12, HM24, HM36, and HM48. Furthermore, the calculations include the quantification of the number of chemical ions adsorbed (n) by just one receptor and the determination of the maximum uptake efficiencies of As (V) ions using the four modified hematite-based adsorbents when it attains its full saturation ($\mathrm{Q}_{\mathrm{sat}}$). The energetic aspects are internal energy ($\mathrm{E}_{\mathrm{int}}$), entropy (Sa), uptake energy (E), and free enthalpy (G). The previously mentioned hypotheses of the established models have been assessed using non-linear regression analyses. A successful completion of the prior investigations was achieved by using multivariable nonlinear regression algorithms in conjunction with the Levenberg–Marquardt iterative approach. Following the obtaining of matching degrees, the adsorption responses of As (V) ions by HM12, HM24, HM36, and HM48 were evaluated and characterized. The substantially corresponding model, the monolayer model of a single active site considering the fitting degree (Fig. 9A–D; Table 3), was used to complete the assignment. Table 3 displays the calculated variables as fitting parameters for the used model.

Material	Model	Parameter	Values		
			293 K	303 K	313 K
HM12	Langmuir	Q_{max} (mg/g)	113.9	105	94.6
		b(L/mg)	7.2×10^{-5}	3.6×10^{-5}	1.67×10^{-5}
		R^2	0.99	0.99	0.99
		X^2	0.031	0.092	0.232
	Freundlich	1/n	0.57	0.63	0.66
		k_F (mg/g)	120.1	115.3	108.4
		R^2	0.98	0.98	0.97
		X^2	0.16	0.39	0.73
	D-R model	β (mol^2/kJ^2)	0.0477	0.0768	0.115
		Q_m (mg/g)	110.6	102.6	94.97
		R^2	0.98	0.97	0.97
		X^2	0.63	1.10	1.18
		E (kJ/mol)	3.2	2.55	2.1
HM24	Langmuir	Q_{max} (mg/g)	125.4	115.3	104
		b(L/mg)	1.66×10^{-4}	1.75×10^{-4}	6.4×10^{-5}
		R^2	0.99	0.99	0.99
		X^2	0.046	0.072	0.43
	Freundlich	1/n	0.60	0.68	0.75
		k_F (mg/g)	132.3	126.1	123.3
		R^2	0.98	0.97	0.97
		X^2	0.234	0.38	0.97
	D-R model	β (mol^2/kJ^2)	0.041	0.058	0.114
		Q_m (mg/g)	119.6	107.6	101.8
		R^2	0.98	0.96	0.95
		X^2	0.67	1.50	1.75
		E (kJ/mol)	3.49	2.93	2.09
HM36	Langmuir	Q_{max} (mg/g)	151.4	133.5	113.6
		b(L/mg)	1.99×10^{-4}	1.68×10^{-4}	2.41×10^{-4}
		R^2	0.99	0.99	0.99
		X^2	0.074	0.17	0.23
	Freundlich	1/n	0.63	0.67	0.72
		k_F (mg/g)	161.3	145.6	125.78
		R^2	0.98	0.98	0.98
		X^2	0.64	0.49	0.51
	D-R model	β (mol^2/kJ^2)	0.0421	0.0549	0.0629
		Q_m (mg/g)	142.8	125.9	105.15
		R^2	0.9707	0.9569	0.9437
		X^2	1.360	1.815	1.943
		E (kJ/mol)	3.44	3.01	2.82
HM48	Langmuir	Q_{max} (mg/g)	138.2	123.3	108.6
		b(L/mg)	1.4×10^{-4}	4.4×10^{-5}	2.3×10^{-5}
		R^2	0.99	0.99	0.99
		X^2	0.14	0.38	0.58
	Freundlich	1/n	0.62	0.63	0.65
		k_F (mg/g)	147.5	135.3	121.8
		R^2	0.98	0.98	0.97
		X^2	0.42	0.92	1.26
	D-R model	β (mol^2/kJ^2)	0.0455	0.0702	0.093
		Q_m (mg/g)	131.7	121.5	109.2
		R^2	0.97	0.96	0.96
		X^2	1.38	1.69	1.75
		E (kJ/mol)	3.31	2.67	2.32

Table 2. The estimated mathematical parameters of the studied classic equilibrium models.

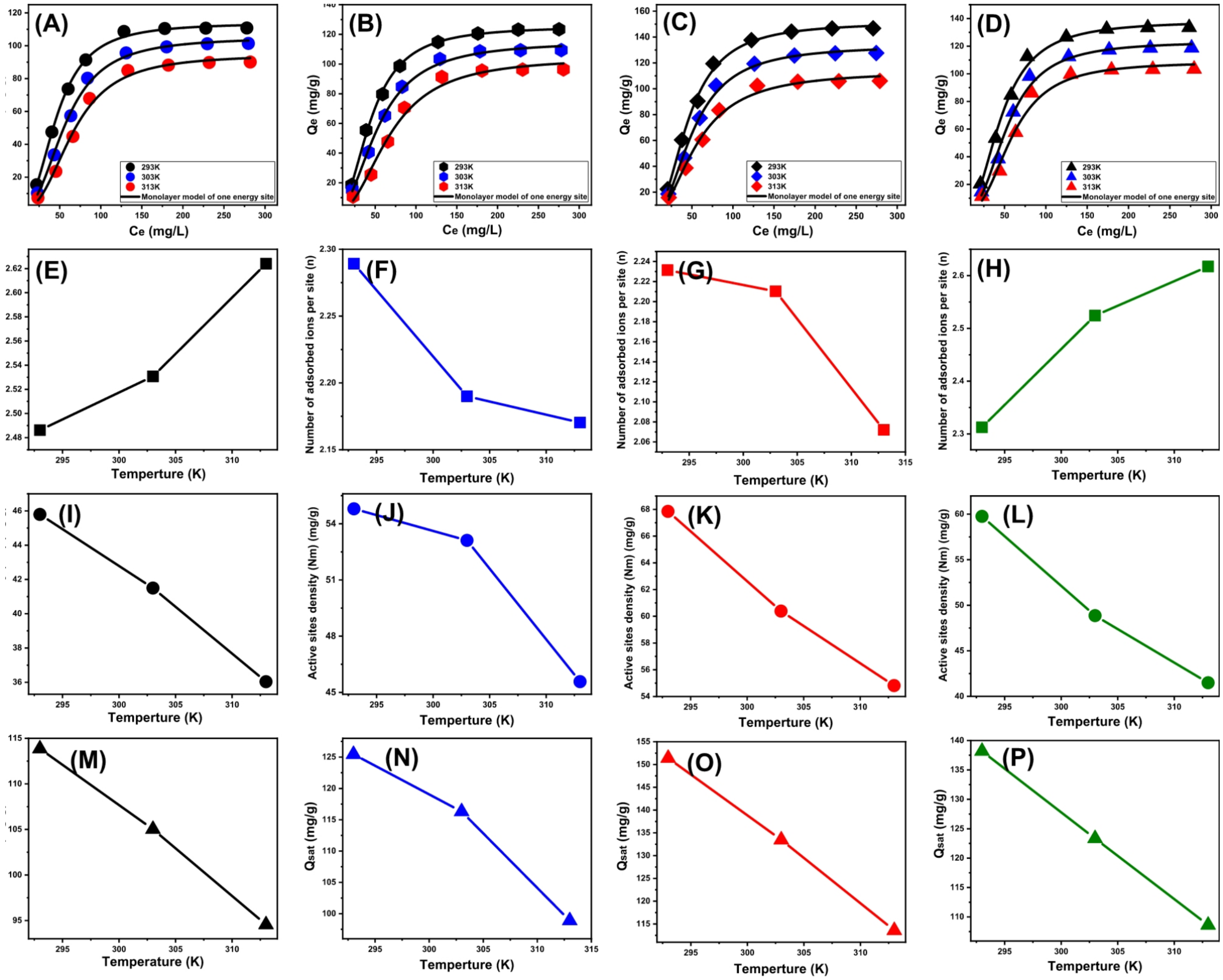

Fig. 9. Fitting of the uptake reactions of As (V) with advanced Monolayer isotherm model with one energy site (**A** (HM12), **B** (HM24), **C** (HM36), and **D** (HM48)), changes in the number of adsorbed As (V) ions (**E** (HM12), **F** (HM24), **G** (HM36), and **H** (HM48)), changes in the occupied sites density (**I** (HM12), **J** (HM24), **K** (HM36), and **L** (HM48)), and changes in the saturation adsorption capacity (**M** (HM12), **N** (HM24), **O** (HM36), and **P** (HM48)).

		n	Nm (mg/g)	Q_{sat} (mg/g)	$C_{1/2}$ (mg/L)	ΔE (kJ/mol)
HM12	393 K	2.49	45.8	113.8	46.4	-7.43
	303 K	2.50	41.5	105.0	57.1	-8.20
	313 K	2.60	36.03	94.6	66.1	-8.85
HM24	393 K	2.28	54.8	125.4	44.8	-7.34
	303 K	2.19	53.1	116.3	53.8	-8.05
	313 K	2.17	45.6	98.9	67.8	-8.92
HM36	393 K	2.23	67.9	151.4	45.5	-7.38
	303 K	2.21	60.4	133.5	51.0	-7.92
	313 K	2.07	54.8	113.6	55.7	-8.41
HM48	393 K	2.31	59.8	138.2	46.3	-7.42
	303 K	2.52	48.9	123.3	53.3	-8.03
	313 K	2.62	41.5	108.6	59.0	-8.56

Table 3. The estimated mathematical parameters of advanced isotherm models.

Steric properties

Number of adsorbed ions per site (n) The mathematical analysis of the n function provides enough data with regard to the arrangement properties of the immobilized As (V) ions across the exterior surface of HM12, HM24, HM36, and HM48. The significance of this includes both the vertical and horizontal arrangements. Moreover, these findings are very significant in understanding the processes that regulate binding reactions, such as multiple dockings or interactions. The uptake of one As (V) ion via multiple uptake sites is significantly affected by the presence of multi-anchorage or multi-docking processes. As a result, the binding mechanisms have values below 1 and indicate the ions' horizontal positioning. Conversely, behaviors with magnitudes above 1 indicate the existence of As (V) ions in non-parallel arrangements, in conjunction with a vertical orientation. Multi-ionic actions typically control the removal pathways for such systems, allowing a single site to accommodate several ions[54,60]. The calculated quantities of n, which indicate the aggregate number of As (V) ions bound to a single uptake site onto the exteriors of the modified derivatives of hematite, ranged from 2.49 to 2.6 (HM12) (Fig. 9E), 2.17 to 2.29 (HM24) (Fig. 9F), 2.07 to 2.23 (HM36) (Fig. 9G), and 2.31 to 2.6 (HM48) (Fig. 9H). The overall number of As (V) ions adsorbed into each site exceeds 1. Therefore, multi-ionic interacting mechanisms successfully achieved the binding of As (V) ions. Each single uptake site on the interfaces of HM12, HM24, HM36, and HM48 had the ability to accommodate up to 3 As (V) ions, which were organized in vertical configurations and non-parallel characteristics.

Regarding the impact of temperature, it can be detected that the synthetic hematite forms display different behaviors in terms of the number of adsorbed As (V) ions per one active site. However, the n values for HM12 and HM48 show a noticeable increment with the tested temperature values; the reported values of HM24 and HM36 exhibit reversible behavior and decline with the temperature. This reflects a declination in the aggregation tendency of the As (V) ions during their interaction with the interfaces of HM12 and HM24. However, it can be expected that there is a considerable increase in the aggregation tendencies of As (V) ions during their interaction with the active sites of HM24 and HM36. Also, this demonstrates the impact of the thermal activation process that might occur prior to the uptake of the arsenic ions into their interfaces[36,60]. Such changes in the reactivity and uptake tendency of each existing site might be assigned to the changes in the morphology and the exposure of the crystalline faces in addition to the associated active sites.

Density of the active sites (Nm) Assessing the density of the active uptake sites for As (V) ions (Fig. 9I–L) could potentially lead to a quantitative determination of the total number of sites filled with As (V) ions (Nm) throughout the interactive interfaces of HM12, HM24, HM36, and HM48 particulates. The values that were determined for Nm at different temperatures for HM12 are 45.8 mg/g at 293 K, 41.5 mg/g at 303 K, and 36.03 mg/g at 313 K (Fig. 9I). These values increased as the modification periods were extended by 24 h and 36 h. The determined values for HM24 are 54.8 mg/g at 293 K, 53.1 mg/g at 303 K, and 45.6 mg/g at 313 K (Fig. 9J), while the estimated values for HM36 are 67.9 mg/g (293 K), 60.4 mg/g (303 K), and 54.8 mg/g (313 K) (Fig. 9K). Extending the modified period for 48 h (HM48) resulted in a slight decrease in the quantities of these existing active sites to 59.8 mg/g (293 K), 48.9 mg/g (303 K), and 41.5 mg/g (313 K) (Fig. 9L). These results illustrate the reported better adsorption efficiency of HM36 for the As (V) ions than the other modified forms. Furthermore, these findings are consistent with the measured surface area and morphological features. The densities of As (V) occupied sites at the interfaces of HM12, HM24, HM36, and HM48 particulates show temperature-sensitive, reversible variations (Fig. 9I–L). The temperature's influence on the activity levels of pre-existing uptake sites could explain the reported behavior[1,61]. The analysis highlights the negative effects of rising temperatures on the extent of occupied sites, which is illustrated by the deactivation of specific operating sites or the reduction in the duration of time needed for these sites to effectively adsorb and retain As (V) ions. Previous studies have attributed comparable trends to the assumed diffusion of adsorbed ions or their desorption from the surfaces of HM12, HM24, HM36, and HM48. The reduction in saturation limitations of heated fluids led to the desorption behavior[62].

Adsorption capacity at the saturation state of (Q_{sat}) The completely saturated adsorption properties of HM12, HM24, HM36, and HM48 (Q_{sat}) present the optimal As (V) uptake capacities, together with the highest tolerance levels. The estimated value of Q_{sat} is affected by two primary factors: the designated density of occupied sites (Nm) and the overall number of As (V) ions bound per site (n). HM12 exhibits maximum adsorption capabilities for As (V) ions of 113.8 mg/g at 293 K, 105 mg/g at 303 K, and 94.6 mg/g at 313 K (Fig. 9M). The determined values for HM24 are 125.4 mg/g at 293 K, 116.3 mg/g at 303 K, and 98.9 mg/g at 313 K (Fig. 9N), while the estimated values for HM36 are 151.4 mg/g (293 K), 133.5 mg/g (303 K), and 113.6 mg/g (313 K) (Fig. 9O). After 48 h (HM48), the values decrease to 138.2 mg/g (293 K), 123.3 mg/g (303 K), and 108.6 mg/g (313 K) (Fig. 9P). The detrimental effects of temperature indicate the exothermic characteristics of the As (V) uptake processes using HM12, HM24, HM36, and HM48. These results demonstrate that greater uptake temperatures promote more thermal collisions, which reduces the efficiency of As (V) adsorption[60]. Furthermore, Q_{sat}'s temperature-dependent observable traits show similarities to the behavior characterized by Nm rather than n for HM12 and HM48, while the trends for HM24 and HM36 match the reported trends for both of them (Fig. 9M–P). The findings indicate that the total amount of interacting sites, rather than the individual binding value of each individual receptor, is the key factor influencing the efficacy of As (V) adsorption via HM12 and HM48. On the other hand, the adsorption performances of HM24 and HM36 were affected significantly by the quantities of existing active adsorption sites as well as the adsorption binding capacity of each site.

Energetic properties

Adsorption energy and mechanism The quantified energy fluctuations (ΔE) during the adsorption processes of As (V) ions may provide valuable insights into the fundamental mechanisms, regardless of their association with chemical or physical reactions. Physical mechanisms show energies below 40 kJ/mol, whereas chemical pathways reveal energetic levels over 80 kJ/mol. These binding energies serve as a significant criterion for classifying different mechanistic responses of physical processes. The physical interactions presented include hydrogen bonding (energy < 30 kJ/mol), dipole bonding interactions (energy range 2–29 kJ/mol), van der Waals forces (energy range 4–10 kJ/mol), electrostatic attraction (energy range 2–50 kJ/mol), and hydrophobic bonding (energy = 5 kJ/mol). The calculation of the uptake energy levels (ΔE) for As (V) ions was conducted using Eq. 5. This equation employs the solubility As (V) ions (S), the gas constant (R = 0.008314 kJ/mol·K), the levels of As (V) ions under half-saturation conditions of HM12, HM24, HM36, and HM48, and an established temperature (T)[63].

$$\Delta E = RTln\left(\frac{S}{C}\right) \tag{5}$$

All of the modified hematite-based adsorbents (HM12, HM24, HM36, and HM48) have As (V) adsorption energies ranging from – 7 to – 9 kJ/mol (Table 3). These ranges are within the established limits for physisorption mechanisms. The quantified values also suggest that electrostatic attraction, hydrogen bonding, dipole interactions, and van der Waals forces are the principal mechanisms facilitating the removal of As (V) ions using HM12, HM24, HM36, and HM48. The negative values of the ΔE data indicate that the binding reactions of As (V) ions were exothermic in nature. Such findings were in agreement with the previous results that proved that uptake of As (V) ions on the surface of iron oxide involved mainly electrostatic attractions, formation of inner-sphere complexes (monodentate and bidentate), and hydrogen bonding, which were represented graphically in Figure S2[64,65].

Entropy The entropy (Sa) corresponding to the adsorption operations of As (V) ions employing HM12, HM24, HM36, and HM48 clearly illustrates the ordered and disordered properties of their exterior interfaces whenever subjected to different levels of As (V) ions, as well as various temperature conditions. The attributes of Sa were demonstrated by using the results derived from Eq. 6, which included the previously determined values for Nm and n, together with the expected levels of As (V) ions during the half-saturation phases of HM12, HM24, HM36, and HM48 (C1/2).

$$\frac{S_a}{K_B} = Nm\left\{ln\left(1+\left(\frac{C}{C_{\frac{1}{2}}}\right)^n\right) - n\left(\frac{C}{C_{\frac{1}{2}}}\right)^n \frac{ln\left(\frac{C}{C_{\frac{1}{2}}}\right)}{1+\left(\frac{C}{C_{\frac{1}{2}}}\right)^n}\right\}[68] \tag{6}$$

The analysis of the resultant graphs reveals a notable decrease in entropy degrees (Sa) upon the adsorption of As (V) ions utilizing HM12, HM24, HM36, and HM48, especially at higher concentrations (Fig. 10A–D). Observations reveal a discernible reduction in the disorder features of HM12, HM24, HM36, and HM48 interfaces when levels of analyzed As (V) ions increase. The entropy factors additionally reveal the enhancement in the effective docking of As (V) ions to the vacant and active binding sites situated on the HM12, HM24, HM36, and HM48 surfaces, regardless of low initial concentrations[61,63,66]. The maximal entropy values for the adsorption of As (V) ions using HM12 were estimated under equilibrium concentrations of 60.2 mg/L (293 K), 63.5 mg/L (303 K), and 66.1 mg/L (313 K) (Fig. 10A). The equilibrium levels of As (V), that correspond to the maximum degree of entropy, were 59.1 mg/L at 293 K, 62 mg/L at 303 K, and 65.4 mg/L at 313 K (Fig. 10B). For the HM36, the detected values are 56.9 mg/L (293 K), 59.5 mg/L (303 K), and 62.8 mg/L (313 K) (Fig. 10C) while for HM48, the values are 58.8 mg/L (293 K), 60.5 mg/L (303 K), and 63.5 mg/L (313 K) (Fig. 10D). Such equilibrium readings are substantially approximated by the concentrations obtained following the HM12, HM24, HM36, and HM48 half-saturation phases. Thus, the existence of leftover binding sites hinders the docking of additional ions. Furthermore, the significant reductions observed in the evaluated entropy levels indicate a substantial decline in the number of available sites, together with a marked drop in the mobility and diffusion properties of the As (V) ions[64].

Internal energy and free enthalpy The study evaluated the internal energy (E_{int}) associated with the binding interactions of As (V) ions using HM12, HM24, HM36, and HM48, along with the free enthalpy (G), taking into account the variations in As (V) contents, as well as the operational temperatures on these properties. The assessment was performed using Eqs. 7 and 8, which derived the results based on the predetermined values for Nm, n, and C1/2, together with the translational partition (Zv)[36].

$$\frac{E_{int}}{K_BT} = nN_m\left[\left(\frac{\left(\frac{C}{C_{1/2}}\right)^n ln\left(\frac{C}{Z_v}\right)}{1+\left(\frac{C}{C_{1/2}}\right)^n}\right) - \left(\frac{n\ln\left(\frac{C}{C_{1/2}}\right)\left(\frac{C}{C_{1/2}}\right)^n}{1+\left(\frac{C}{C_{1/2}}\right)^n}\right)\right] \tag{7}$$

$$\frac{G}{K_BT} = nN_m\frac{\ln\left(\frac{C}{Z_v}\right)}{1+\left(\frac{C_{1/2}}{C}\right)^n} \tag{8}$$

The examined fluctuations in E_{int} in terms of the removal processes of As (V) ions using HM12, HM24, HM36, and HM48 exhibit negatively signed values. The results showed a significant reduction in E_{int} whenever the

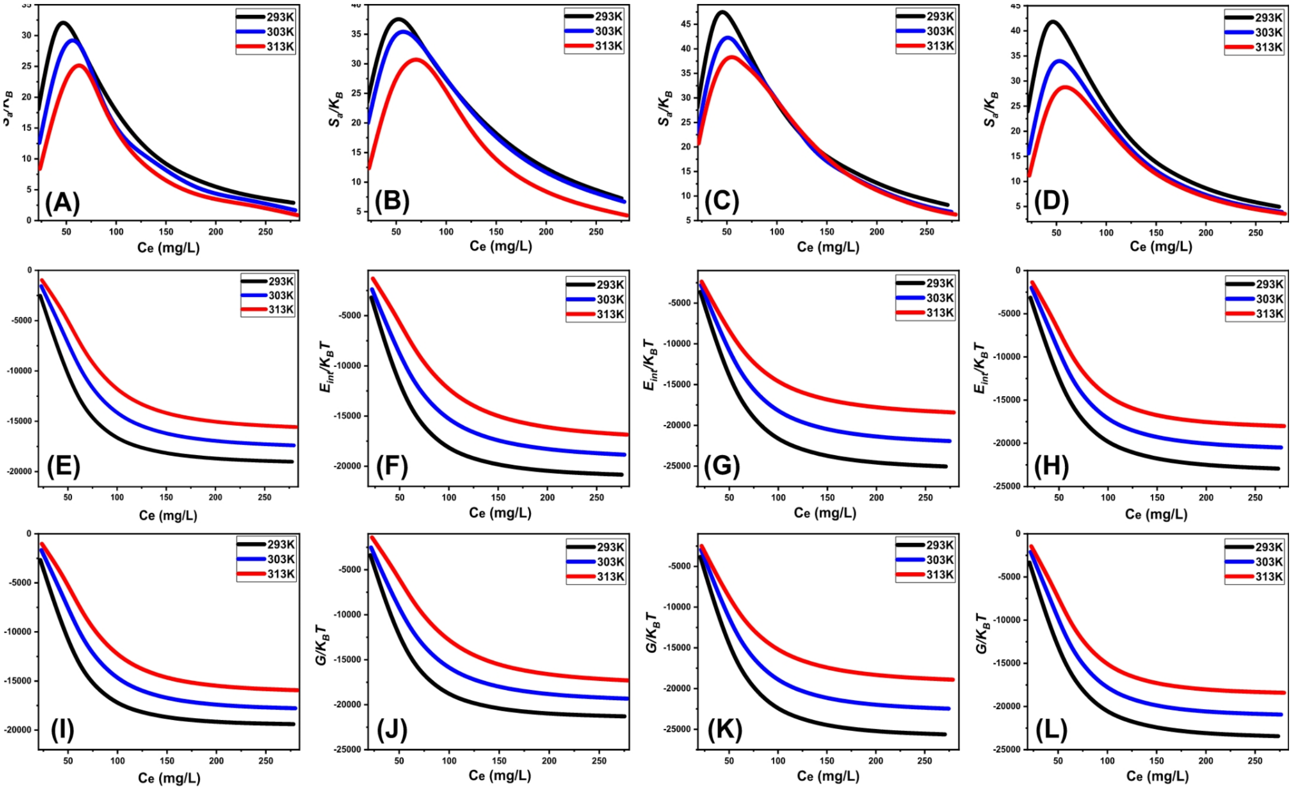

Fig. 10. Change in the thermodynamic *functions* during the uptake of As (V) ions by modified hematite based adsorbents including entropy (**A** (HM12), **B** (HM24), **C** (HM36), and **D** (HM48)), internal energy (**E** (HM12), **F** (HM24), **G** (HM36), and **H** (HM48)), and enthalpy (**I** (HM12), **J** (HM24), **K** (HM36), and **L** (HM48)).

temperature increases from 293 to 313 K (Fig. 10E–H). This investigation confirms the spontaneous and exothermic properties of both ions' adsorption reactions using the modified hematite adsorbents. The enthalpy assessments and activities display similar characteristics and criteria corresponding to those of the internal energy behaviors. The G data exhibit negative trends and demonstrate a reversible relationship with the specific uptake temperature (Fig. 10I–L). This signifies a decrease in feasibility characteristics and corroborates the exothermic nature and spontaneous features of the adsorption reactions of As (V) ions employing HM12, HM24, HM36, and HM48.

Solid dosage

The influence of varying HM36 dosages on the adsorption efficiency of As(V) ions was systematically evaluated within a concentration range of 0.2 g/L to 0.6 g/L. The adsorption experiments were conducted under controlled conditions, maintaining a solution volume of 100 mL, an initial As(V) concentration of 50 mg/L, a pH of 5, a temperature of 293 K, and a contact time of 24 h. The results demonstrated a significant enhancement in As(V) removal efficiency with increasing HM36 dosage, which can be attributed to the greater availability of active sites and expanded surface area, thereby facilitating improved ion adsorption. However, beyond a dosage of 0.5 g/L, the removal efficiency exhibited a saturation trend, indicating that the adsorbent had reached its maximum adsorption capacity. Additional increases in HM36 dosage beyond this threshold yielded only marginal improvements, suggesting that the available adsorption sites had become fully occupied. The experimental findings revealed a progressive increase in removal efficiency from 24.2% at 0.2 g/L to 40.6% at 0.3 g/L, 58.7% at 0.4 g/L, 74.3% at 0.5 g/L, and reaching 80.6% at 0.6 g/L (Fig. S3).

Effect of coexisting cations and anions

The impact of coexisting cations (Cd (II), Pb (II), Ni (II), Co (II), and, Cr (VI)) and anions NO_3^-, SO_4^{2-}, PO_4^{3-}, and CO_3^{2-} on the adsorption efficiency and selectivity of HM36 for As (V) ions was systematically evaluated under controlled experimental conditions. The experiments were conducted with a solution volume of 100 mL, an initial concentration of 100 mg/L (50% As (V) and 50% coexisting ions), pH 5, HM36 dosage of 0.2 g/L, temperature of 293 K, and a contact time of 24 h (Fig. 11).

The studied anions demonstrated minimal interference with As (V) adsorption by HM36 (Fig. 11A). Among these, PO_4^{3-} and CO_3^{2-} showed relatively higher competition compared to NO_3^- and SO_4^{2-}. This is likely due to the chemical and physicochemical similarity between As (V) and PO_4^{3-}, which facilitates competition for binding sites[67]. Additionally, PO_4^{3-} forms inner-sphere complexes with hydroxyl functional groups, intensifying its competitive effect[68]. A similar mechanism applies to CO_3^{2-}, which shares comparable structural attributes

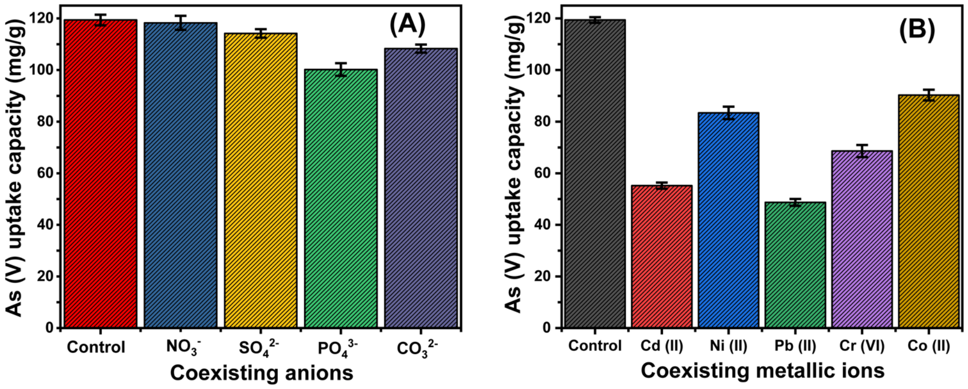

Fig. 11. Effect of coexisting *chemical* anions (**A**) and metallic ions (**B**) on the adsorption performances of HM36 for As (V).

with As (V)[68]. In contrast, NO_3^- and SO_4^{2-} form outer-sphere complexes, resulting in lower competitive interactions during the adsorption of As (V), which primarily involves inner-sphere complex formation[67,68]. For the cations Cd (II), Pb (II), Ni (II), Co (II), and, Cr (VI) their presence significantly reduced HM36's adsorption capacity for As (V) (Fig. 11B). The retention capacities in the presence of these competing ions were reduced to 55.2 mg/g (Cd (II), 48.7 mg/g (Pb (II)), 83.4 mg/g (Ni (II)), 91.5 mg/g (Co (II)), and 90.3 mg/g (Cr (VI)), respectively. Despite these adverse effects, the retention efficiency under these conditions suggests the potential applicability of HM36 in practical remediation processes.

Effect of water type

To assess the feasibility of employing HM36 for purifying raw water, comprehensive studies were conducted to evaluate its adsorption performance for As (V) removal from tap water, groundwater, and sewage water (Table S2). The adsorption capacities of HM36 for As (V) were determined to be 119.5 mg/g for distilled water, 111.4 mg/g for tap water, 105.3 mg/g for groundwater, and 97.4 mg/g for sewage water (Fig. S4). Notably, even at treatment concentrations as high as 100 mg/L—significantly exceeding typical environmental levels—HM36 demonstrated high removal efficiency. These findings confirm the effectiveness of HM36 in treating real-world contaminated water. The observed reduction in adsorption capacity across different water types (from distilled water to sewage water) is likely attributable to the presence of additional chemical constituents in natural water sources, which compete with As (V) during the adsorption process.

Recyclability

The reusability of HM36 was evaluated after alkaline washing (20 mL of 0.05 M NaOH at 20 °C for 120 min), followed by rinsing with distilled water until neutralization and drying at 60 °C for 8 h. This process was repeated across five adsorption cycles. Adsorption experiments were conducted with a solution volume of 100 mL, As (V) concentration of 300 mg/L, pH 5, HM36 dosage of 0.2 g/L, temperature of 293 K, and contact time of 24 h. The HM36 structure demonstrated substantial reusability, with adsorption capacities of 146.7 mg/g, 140.2 mg/g, 132.6 mg/g, 114.7 mg/g, and 98.5 mg/g over cycles 1 through 5, respectively (Fig. S5). The gradual decline in retention capacity with repeated cycles can be attributed to the progressive accumulation of adsorbed As (V) complexes on active sites, reducing available binding functionality. The reduced efficiency observed with repeated use may result from the persistent formation of complexes between the adsorbed ions and HM36's chemical structure. However, the low leaching of iron content (<0.001 mg/L) during adsorption tests across the studied pH range confirms the structural stability of HM36 and its minimal contribution to secondary contamination. These findings highlight HM36's environmental value and its potential for safe and effective water remediation.

Comparison study

The adsorption performances of HM12, HM24, HM36, and HM48 for As (V) were evaluated against various organic and ion-organic adsorbents, as detailed in Table 4. The findings demonstrate that the modified products especially HM36 exhibit superior adsorption properties compared to most materials listed. This highlights its potential as a cost-effective and environmentally sustainable solution for treating wastewater containing diverse soluble organic and inorganic contaminants. Moreover, the synthetic structure offers economic advantages, requiring lower dosages and shorter contact times to achieve higher removal efficiencies than many alternative adsorbents.

Conclusion

This study successfully demonstrated the transformation of natural hematite ore into highly efficient two-dimensional (2D) hematite nanorods via a simple and cost-effective hydrothermal modification process. The structural and morphological transformation of natural hematite into nanorods was achieved through alkaline treatment at different durations (12 h, 24 h, 36 h, and 48 h). The HM36 sample exhibited the most effective

Adsorbent	$Q_{(max)}$ (mg/g)	References
$ZrO(OH)_2$/CNTs	124.5	[69]
Goethite/goethite P	34.12	[70]
GO/$CuFe_2O_4$ foam	124.69	[71]
ZnO/ AlSBA-15	123.99	[72]
Iron oxide nanoparticle	22.91	[73]
Chitosan-coated biosorbent	96.46	[74]
FeOx-GO	113	[75]
0.26γ-Fe_2O_3/SBA-15	23.09	[76]
Magnetite–graphene–LDH	73.14	[77]
Silica-sand/cationized-starch	76.63	[78]
Fe3O4:CuO nanocomposite	62.6	[79]
Magnetite-partially reduced GO	131.9	[80]
Cross-linked chitosan	34.12	[81]
Zirconium-nanoscale carbon	110	[82]
Iron oxide grafted TNTs	90.96	[83]
Iron–chitosan flakes	22.47	[84]
HM12	113.8	This study
HM24	125.4	This study
HM36	151.4	This study
HM48	138.2	This study

Table 4. Comparison between the As (V) retention capacity of HM36 and other studied adsorbents.

conversion, resulting in well-developed nanorods with the highest specific surface area (154.7 m^2/g), which directly correlated with enhanced adsorption performance. The uptake capacity of As (V) ions was highest for HM36 (151.4 mg/g), outperforming other modified forms (HM12: 113.8 mg/g, HM24: 125.4 mg/g, and HM48: 138.2 mg/g). The advanced equilibrium investigations based on statistical physics models further validated the superior adsorption properties of HM36, highlighting its higher density of active adsorption sites (Nm = 67.9 mg/g). The ability of each site to accommodate up to three As (V) ions suggests a multi-ionic interaction mechanism, facilitating the vertical ordering of adsorbed ions at the adsorbent surface. Additionally, the kinetic investigations confirmed that the adsorption process predominantly followed a pseudo-first-order model, suggesting a physisorption-dominated mechanism. The adsorption energy, estimated through both classical (< 4 kJ/mol) and advanced models (< 9 kJ/mol), reaffirmed the physical nature of the uptake process, primarily governed by electrostatic attractions, hydrogen bonding, and van der Waals forces. Thermodynamic evaluations indicated that As (V) adsorption onto HM36 was spontaneous and exothermic, demonstrating the material's feasibility for practical applications. Furthermore, the recyclability assessment confirmed that HM36 retains its adsorption efficiency over multiple cycles, underscoring its suitability for sustainable water treatment applications. The combination of simple synthesis, cost-effectiveness, high removal efficiency, and structural stability suggests that HM36 can serve as a promising adsorbent for the practical remediation of As (V)-contaminated water sources, particularly in industrial and agricultural wastewater treatment settings. Future research could explore the scalability of this approach and its application to other contaminants to broaden its environmental and industrial impact.

Data availability

The data will be available up on request to corresponding author.

Received: 14 October 2024; Accepted: 17 March 2025

References

1. Yang, X. et al. Insight into the adsorption and oxidation activity of a ZnO/ piezoelectric quartz core-shell for enhanced decontamination of ibuprofen: steric, energetic, and oxidation studies. *Chem. Eng. J.* **431**, 134312 (2022).
2. Zourou, A. et al. Graphene oxide-CuFe2O4 nanohybrid material as an adsorbent of Congo red dye. *Carbon Trends* **7**, 100147 (2022).
3. Ighnih, H. et al. Synergistic enhancement of pollutant removal from water by using BiOCl/BiOBr heterojunction on clay surface and sunlight irradiation. *J. Water Process Eng.* **58**, 104766 (2024).
4. Kusuma, H. S., Illiyanasafa, N., Jaya, D. E. C., Darmokoesoemo, H. & Putra, N. R. Utilization of the microalga Chlorella vulgaris for mercury bioremediation from wastewater and biomass production. *Sustain. Chem. Pharm.* **37**, 101346 (2024).
5. Wu, J. et al. Emulsion synthesis of cellulose/lanthanum alginate/La (III) composite microspheres for efficient and selective adsorption of phosphate. *Chem. Eng. J.* **488**, 150949 (2024).
6. Salam, M. A. et al. Synthesis of zeolite/geopolymer composite for enhanced sequestration of phosphate ($PO_4^{3-)}$ and ammonium (NH4+) ions; equilibrium properties and realistic study. *J. Environ. Manag.* **300**, 113723 (2021).
7. Shi, W. et al. Enhanced phosphate removal by zeolite loaded with Mg–Al–La ternary (hydr)oxides from aqueous solutions: Performance and mechanism. *Chem. Eng. J.* **357**, 33–44 (2019).

8. Che, N. et al. Adsorption of phosphate onto agricultural waste biochars with ferrite/manganese modified-ball-milled treatment and its reuse in saline soil. *Sci. Total Environ.* **915**, 169841 (2024).
9. Mutar, R. F. & Saleh, M. A. Optimization of arsenic ions adsorption and removal from hospitals wastewater by nano-bentonite using central composite design. *Mater. Today Proc.* **60**, 1248–1256 (2021).
10. Wang, C., Dai, Y., Fu, X., Lu, H. & Zhang, J. A novel layer-layer crossed structure of bentonite/g-C3N4 for enhanced photocatalytic oxidation of arsenic(III) in a wide pH range. *Surf. Interfaces* **26**, 101365 (2021).
11. Yoon, K., Cho, D.-W., Bhatnagar, A. & Song, H. Adsorption of As(V) and Ni(II) by Fe-Biochar composite fabricated by co-pyrolysis of orange peel and red mud. *Environ. Res.* **188**, 109809 (2020).
12. Das, S., Paul, S. R. & Debnath, A. Methyl red dye abatement from aqueous solution using calcium ferrite and manganese ferrite magnetic nanocomposite: kinetics and isotherm study. *Proc. Earth Environ. Sci.* https://doi.org/10.1007/978-3-031-37596-5_2 (2023).
13. Nandi, D. et al. Arsenic removal from water by graphene nanoplatelets prepared from nail waste: A physicochemical study of adsorption based on process optimization, kinetics, isotherm and thermodynamics. *Environ. Nanotechnol. Monit. Manag.* **16**, 100564 (2021).
14. Salam, M. A. et al. Synthesis and characterization of green ZnO@polynaniline/bentonite tripartite structure (GZn@PN/BE) as adsorbent for As (V) ions: Integration. *Steric Energ. Prop. Polym.* **14**, 2329 (2022).
15. Li, Y., Xiang, K., Qu, G. & Li, R. Preparation of ionic liquid modified graphene composites and their adsorption mechanism of arsenic (V) in aqueous solution. *Environ. Sci. Pollut. Res.* **31**, 16401–16412 (2024).
16. Paul, S. R., Das, S., Debnath, A. & Misra, T. K. Boosted adsorptive removal of eosin yellow dye from aqueous solution with C–ZnO nanoparticles: optimization of process parameters. *J. Dispers. Sci. Technol.* 1–17 (2024).
17. Karakoç, V. & Erçağ, E. New generation nanoadsorbents and conventional techniques for arsenic removal from waters. *J. Turk. Chem. Soc. Sect. Chem.* **11**, 845–868 (2024).
18. Deb, A., Das, S. & Debnath, A. Fabrication and characterization of organometallic nanocomposite for efficient abatement of dye laden wastewater: CCD optimization, adsorption mechanism, co-existing ions, and cost analysis. *Chem. Phys. Lett.* **830**, 140820 (2023).
19. Albukhari, S. M., Salam, M. A. & Abukhadra, M. R. Effective retention of inorganic Selenium ions (Se (VI) and Se (IV)) using novel sodalite structures from muscovite; characterization and mechanism. *J. Taiwan Inst. Chem. Eng.* **120**, 116–126 (2021).
20. Das, S., Pal, A. & Debnath, A. Polyaniline-coated magnesium ferrite nanocomposite: Synthesis, characterization, fabrication cost analysis and dye sorption behavior with scale-up design. *ChemistrySelect* **8**, e202300928 (2023).
21. Ifa, L. et al. Techno-economics of coconut coir bioadsorbent utilization on free fatty acid level reduction in crude palm oil. *Heliyon* https://doi.org/10.1016/j.heliyon.2022.e09146 (2022).
22. Sun, X. et al. Steric and energetic studies on the influence of cellulose on the adsorption effectiveness of Mg trapped hydroxyapatite for enhanced remediation of chlorpyrifos and omethoate pesticides. *Int. J. Biol. Macromol.* **265**, 130711 (2024).
23. Chen, Y. et al. Hydroxyapatite modified sludge-based biochar for the adsorption of Cu2+ and Cd2+: adsorption behavior and mechanisms. *Bioresour. Technol.* **321**, 124413 (2021).
24. Chen, W., Guo, G., Huang, L., Ouyang, L. & Shuai, Q. Facet-dependent adsorption of aromatic organoarsenicals on hematite: The mechanism and environmental impact. *J. Hazardous Mater.* **464**, 132976 (2024).
25. Tao, Z., Zhou, Q., Zheng, T., Mo, F. & Ouyang, S. Iron oxide nanoparticles in the soil environment: Adsorption, transformation, and environmental risk. *J. Hazard. Mater.* **459**, 132107 (2023).
26. Mbachu, C. A. et al. Green synthesis of iron oxide nanoparticles by Taguchi design of experiment method for effective adsorption of methylene blue and methyl orange from textile wastewater. *Results Eng.* **19**, 101198 (2023).
27. Keshta, B. E., Gemeay, A. H. Sinha, S., Elsharkawy, F., Hassan, N. & Arora, C. State of the art on the magnetic iron oxide nanoparticles: synthesis, functionalization, and applications in wastewater treatment. Results Chem. (2024).
28. Talibawo, J., Kyesmen, P. I., Cyulinyana, M. C. & Diale, M. Facile Zn and Ni Co-doped hematite nanorods for efficient photocatalytic water oxidation. *Nanomaterials* **12**, 2961 (2022).
29. Dehmani, Y. et al. Removal of phenol from aqueous solution by adsorption onto hematite (α-Fe2O3): Mechanism exploration from both experimental and theoretical studies. *Arab. J. Chem.* **13**, 5474–5486 (2020).
30. Rajendran, S. et al. Nanostructured iron oxides: Structural, optical, magnetic, and adsorption characteristics for cleaning industrial effluents. *Crystals* **13**, 472 (2023).
31. Gulzar, A. et al. In vitro and in vivo MRI imaging and photothermal therapeutic properties of Hematite (α-Fe2O3) Nanorods. *J. Mater. Sci. Mater. Med.* https://doi.org/10.1007/s10856-021-06636-1 (2022).
32. Li, Z. et al. Surface engineering of hematite nanorods photoanode towards optimized photoelectrochemical water splitting. *J. Colloid Interface Sci.* **626**, 879–888 (2022).
33. Kim, D. H. et al. Au decoration of vertical hematite nanotube arrays for further selective detection of acetone in exhaled breath. *Sens. Actuator B Chem.* **274**, 587–594 (2018).
34. Cao, S. et al. Insights into the facet-dependent adsorption of phenylarsonic acid on hematite nanocrystals. *Environ. Sci. Nano* **6**, 3280–3291 (2019).
35. Wang, W. et al. Facet-dependent adsorption of aluminum(iii) on hematite nanocrystals and the influence on mineral transformation. *Environ. Sci. Nano* **9**, 2073–2085 (2022).
36. Dhaouadi, F. et al. Adsorption mechanism of Zn^{2+}, Ni^{2+}, Cd^{2+}, and Cu^{+2} ions by carbon-based adsorbents: Interpretation of the adsorption isotherms via physical modeling. *Environ. Sci. Pollut. Res.* **28**, 30943–30954 (2021).
37. Dissanayake, D. M. S. N., Mantilaka, M. M. M. G. P.G., Palihawadana, T. C., Chandrakumara, G. T. D., De Silva, R. T., Pitawala, H. M. T. G. A., De Silva, K. M. N. & Amaratunga, G. A. J. Facile and low-cost synthesis of pure hematite (α-Fe2O3) nanoparticles from naturally occurring laterites and their superior adsorption capability towards acid-dyes. RSC Adv. **9**, 21249–21257 (2019).
38. Tatarchuk, T., Shyichuk, A., Danyliuk, N., Lapchuk, I. & Macyk, W. Water disinfection using hydrogen peroxide with fixed bed hematite catalyst—Kinetic and activity studies. *Environ. Sci. Pollut. Res.* **31**, 26592–26605 (2024).
39. Khorshidi, N. & Azadmehr, A. R. Competitive adsorption of Cd (II) and Pb (II) ions from aqueous solution onto Iranian hematite (Sangan mine): Optimum condition and adsorption isotherm study. *Desalination Water Treat.* **58**, 106–119 (2017).
40. Bai, S. et al. Adsorption of sodium oleate at the microfine hematite/aqueous solution interface and its consequences for flotation. *Int. J. Min. Sci. Technol.* **33**, 105–113 (2023).
41. Xie, H. et al. Effect of the occurrence state of magnesium in talc on the adsorption of Pb(II). *J. Alloys Compounds* **887**, 161288 (2021).
42. Jiang, Y. et al. Synthesis of chitosan/MCM-48 and β-cyclodextrin/MCM-48 composites as bio-adsorbents for environmental removal of Cd^{2+} ions; kinetic and equilibrium studies. *React. Funct. Polym.* **154**, 104675 (2020).
43. Yin, Y. et al. Adsorption of arsenic by activated charcoal coated zirconium-manganese nanocomposite: Performance and mechanism. *Colloids Surf. Physicochem. Eng. Asp.* **575**, 318–328 (2019).
44. Sun, J., Zhang, X., Zhang, A. & Liao, C. Preparation of Fe–Co based MOF-74 and its effective adsorption of arsenic from aqueous solution. *J. Environ. Sci.* **80**, 197–207 (2018).
45. Salam, M. A., Abukhadra, M. R. & Mostafa, M. Effective decontamination of As(V), Hg(II), and U(VI) toxic ions from water using novel muscovite/zeolite aluminosilicate composite: Adsorption behavior and mechanism. *Environ. Sci. Pollut. Res.* **27**, 13247–13260 (2020).

46. Neolaka, Y. A. B., Supriyanto, G., Darmokoesoemo, H. & Kusuma, H. S. Characterization, kinetic, and isotherm data for Cr(VI) removal from aqueous solution by Cr(VI)-imprinted poly(4-VP-co-MMA) supported on activated Indonesia (Ende-Flores) natural zeolite structure. *Data Brief.* **17**, 969–979 (2018).
47. Neolaka, Y. A. B. et al. Evaluation of magnetic material IIP@ GO-Fe3O4 based on Kesambi wood (Schleichera oleosa) as a potential adsorbent for the removal of Cr(VI) from aqueous solutions. *React. Funct. Polym.* **166**, 105000 (2021).
48. Neolaka, Y. A. B. et al. Efficiency of activated natural zeolite- based magnetic composite (ANZ-Fe3O4) as a novel adsorbent for removal of Cr(VI) from wastewater. *J. Mater. Res. Technol.* **18**, 2896–2909 (2022).
49. El-Sherbeeny, A. M. et al. Effective retention of radioactive Cs+ and Ba2+ ions using β-cyclodextrin functionalized diatomite (β-CD/D) as environmental adsorbent; characterization, application, and safety. *Surf. Interfaces.* **26**, 101434 (2021).
50. AbdelSalam, M., Mokhtar, M., Albukhari, S. M., Baamer, D. F., Palmisano, L., Jaremko, M., Abukhadra, M. R. Synthesis and characterization of green ZnO@ polynaniline/bentonite tripartite structure (G. Zn@ PN/BE) as adsorbent for As (V) ions: Integration, Steric, and energetic properties. *Polymers* **14**(12), 2329 (2022).
51. El Qada, E. Kinetic behavior of the adsorption of malachite green using jordanian diatomite as adsorbent. *Jordan. J. Eng. Chem. Ind. (JJECI) Res. Pap.* **3**(1), 1 (2020).
52. Lin, X. et al. Facile preparation of dual La-Zr modified magnetite adsorbents for efficient and selective phosphorus recovery. *Chem. Eng. J.* **413**, 127530 (2021).
53. Rahaman, Md. H. et al. Preparation, characterization, and adsorption kinetics of graphene oxide/chitosan/carboxymethyl cellulose composites for the removal of environmentally relevant toxic metals. *Int. J. Biol. Macromol.* **257**, 128357 (2023).
54. Sayed, I. R., Farhan, A. M., AlHammadi, A. A., El-Sayed, M.I., Abd El-Gaied, I. M., El-Sherbeeny, A. M., Al Zoubi, W., Ko, Y. G., & Abukhadra, M. R. Synthesis of novel nanoporous zinc phosphate/hydroxyapatite nano-rods (ZPh/HPANRs) core/shell for enhanced adsorption of Ni^{2+} and Co^{2+} ions: Characterization and application. *J. Mol. Liq.* **360**, 119527 (2022).
55. Neolaka, Y. A. B. et al. Potential of activated carbon from various sources as a low-cost adsorbent to remove heavy metals and synthetic dyes. *Results Chem.* **5**, 100711 (2023).
56. Sherlala, A., Raman, M. M. & Bello, A. Buthiyappan, Adsorption of arsenic using chitosan magnetic graphene oxide nanocomposite. *J. Environ. Manag.* **246**, 547–556 (2019).
57. Jasper, E. E., Ajibola, V. O. & Onwuka, J. C. Nonlinear regression analysis of the sorption of crystal violet and methylene blue from aqueous solutions onto an agro-waste derived activated carbon. *Appl. Water Sci.* **10**(6), 1–11 (2020).
58. Ahmed, A. M., Saad, I., Rafea, M. A. & Abukhadra, M. R. Synergetic and advanced isotherm investigation for the enhancement influence of zeolitization and β-cyclodextrin hybridization on the retention efficiency of U(vi) ions by diatomite. *RSC Adv.* **14**, 8752–8768 (2024).
59. Das, S., Paul, S. R. & Debnath, A. Enhanced performance of Lagerstroemia speciosa seed biochar and polypyrrole composite for the sequestration of emerging contaminant from wastewater sample: Case study of ofloxacin drug. *J. Water Process Eng.* **64**, 105699 (2024).
60. Mobarak, M., Ali, R. A. & Seliem, M. K. Chitosan/activated coal composite as an effective adsorbent for Mn (VII): Modeling and interpretation of physicochemical parameters. *Int. J. Biol. Macromol.* **186**, 750–758 (2021).
61. Sellaoui, L., Ali, J., Badawi, M., Bonilla-Petriciolet, A. & Chen, Z. Understanding the adsorption mechanism of Ag+ and Hg2+ on functionalized layered double hydroxide via statistical physics modeling. *Appl. Clay Sci.* **198**, 105828 (2020).
62. Ahmed, A. M., Nasser, N., Rafea, M. A. & Abukhadra, M. R. Effective retention of cesium ions from aqueous environment using morphologically modified kaolinite nanostructures: Experimental and theoretical studies. *RSC Adv.* **14**, 3104–3121 (2024).
63. Dhaouadi, F. et al. Statistical physics interpretation of the adsorption mechanism of Pb^{2+}, Cd^{2+} and Ni^{2+} on chicken feathers. *J. Mol. Liq.* **319**, 114168 (2020).
64. Darezereshki, E., Darban, A. K., Abdollahy, M. & Jamshidi-Zanjani, A. Influence of heavy metals on the adsorption of arsenate by magnetite nanoparticles: Kinetics and thermodynamic. *Environ. Nanotechnol. Monit. Manag.* **10**, 51–62 (2018).
65. Verma, L. & Singh, J. Arsenic adsorption from aqueous solution and groundwater using monometallic (Fe) and bimetallic (Fe/Mn) Tectona biochar synthesized from plant refuse: Mechanism, isotherm, and kinetic study. *Environ. Eng. Res.* **28**, 220110 (2022).
66. Sellaoui, L. et al. Experimental and theoretical studies of adsorption of ibuprofen on raw and two chemically modified activated carbons: New physicochemical interpretations. *RSC Adv.* **6**(15), 12363–12373 (2016).
67. He, X. et al. Exceptional adsorption of arsenic by zirconium metal-organic frameworks: Engineering exploration and mechanism insight. *J. Colloid Interface Sci.* **539**, 223–234 (2019).
68. Yin, Y. et al. Adsorption of arsenic by activated charcoal coated zirconium-manganese nanocomposite: Performance and mechanism. *Colloids Surf. A Physicochem. Eng. Asp.* **575**, 318–328 (2019).
69. Liu, D. et al. As (III) and As (V) adsorption on nanocomposite of hydrated zirconium oxide coated carbon nanotubes. *J. Colloid Interface Sci.* **511**, 277–284 (2018).
70. Ramirez-Muñiz, K., Perez-Rodriguez, F. & Rangel-Mendez, R. Adsorption of arsenic onto an environmental friendly goethite-polyacrylamide composite. *J. Mol. Liq.* **264**, 253–260 (2018).
71. Wu, L. K. et al. Highly porous copper ferrite foam: a promising adsorbent for efficient removal of As (III) and As (V) from water. *J. Hazard. Mater.* **347**, 15–24 (2018).
72. Mahato, B. N., Krithiga, T. & Thangam, M. M. Rapid adsorption of As (V) from aqueous solution by ZnO embedded in mesoporous aluminosilicate nanocomposite adsorbent: Parameter optimization, kinetic, and isotherms studies. *Surf. Interfaces* **23**, 100636 (2021).
73. Lee, C. G. et al. Arsenic (V) removal using an amine-doped acrylic ion exchange fiber: kinetic, equilibrium, and regeneration studies. *J. Hazard. Mater.* **325**, 223–229 (2017).
74. Boddu, V. M., Abburi, K., Talbott, J. L., Smith, E. D. & Haasch, R. Removal of arsenic (III) and arsenic (V) from aqueous medium using chitosan-coated biosorbent. *Water Res.* **42**(3), 633–642 (2008).
75. Su, H., Ye, Z. & Hmidi, N. High-performance iron oxide–graphene oxide nanocomposite adsorbents for arsenic removal. *Colloids Surf. A Physicochem. Eng. Asp.* **522**, 161–172 (2017).
76. Peng, X. et al. One-step and acid free synthesis of γ-Fe_2O_3/SBA-15 for enhanced arsenic removal. *Microporous Mesoporous Mater.* **258**, 26–32 (2018).
77. Wu, X.-L., Wang, L., Chen, C.-L., Xu, A.-W. & Wang, X.-K. Water-dispersible magnetite-graphene-LDH composites for efficient arsenate removal. *J. Mater. Chem.* **21**, 17353 (2011).
78. Li, P., Gao, B., Li, A. & Yang, H. Highly selective adsorption of dyes and arsenate from their aqueous mixtures using a silica-sand/cationized-starch composite. *Microporous Mesoporous Mater.* **263**, 210–219 (2018).
79. Wu, K. et al. Magnetic Fe3O4@CuO nanocomposite assembled on graphene oxide sheets for the enhanced removal of arsenic(III/V) from water. *Appl. Surf. Sci.* **466**, 746–756 (2018).
80. Bobb, J. A., Awad, F. S., Moussa, S. & El-Shall, M. S. Laser synthesis of magnetite-partially reduced graphene oxide nanocomposites for arsenate removal from water. *J. Mater. Sci.* **55**, 5351–5363 (2020).
81. Zeng, H. et al. Selective adsorption of arsenic by water treatment residuals cross-linked chitosan in co-existing oxyanions competition system. *Environ. Res.* **263**, 120192 (2024).
82. Mahanta, N. & Chen, J. P. A novel route to the engineering of zirconium immobilized nano-scale carbon for arsenate removal from water. *J. Mater. Chem. A* **1**, 8636 (2013).
83. Wang, Y., Liu, W., Wang, T. & Ni, J. Arsenate adsorption onto Fe-TNTs prepared by a novel water–ethanol hydrothermal method: Mechanism and synergistic effect. *J. Colloid Interface Sci.* **440**, 253–262 (2014).

84. Gupta, A., Chauhan, V. S. & Sankararamakrishnan, N. Preparation and evaluation of iron–chitosan composites for removal of As(III) and As(V) from arsenic contaminated real life groundwater. *Water Res.* **43**, 3862–3870 (2009).

Acknowledgements

The authors acknowledge Princess Nourah bint Abdulrahman University Researchers Supporting Project number (PNURSP2025R737), Princess Nourah bint Abdulrahman University, Riyadh, Saudi Arabia.

Author contributions

1. Dina Mostafa : Methodology, Visualization, Data curation, Formal analysis, Writing -original draft, Writing – review & editing 2. Nabila Shehata : Conceptualization, supervision, validation, Writing – review & editing 3. Mashael D. Alqahtani: Formal analysis, Funding, Data curation, methodology, software, validation, Writing—original draft, Writing – review & editing 4. May N. Bin Jumah: Data curation, validation, Writing – review & editing 5. Nahaa M. Alotaibi:Methodology, visualization, Writing – review & editing 6.Noof A. Alenazi: Methdology, Data curation, validation, Writing – review & editing 7. Hassan A. Rudayni: Data curation, validation, Writing – review & editing 8. Ahmed A. Allam: Conceptualization, Resources, validation, Writing – review & editing 9. Wail Al Zoubi: Conceptualization, Resources, validation, Writing – review & editing 10. Mostafa R. Abukhadra: Conceptualization, Formal analysis, supervision, Resources, Data curation, Visualization, methodology, validation, Writing—original draft, Writing – review & editing.

Declarations

Competing interests

The authors declare no competing interests.

Additional information

Supplementary Information The online version contains supplementary material available at https://doi.org/10.1038/s41598-025-94802-8.

Correspondence and requests for materials should be addressed to W.A.Z.

Reprints and permissions information is available at www.nature.com/reprints.